7

Nitrogen abundance in the X-ray halos of clusters and groups of galaxies

Junjie Mao, J. de Plaa, J. S. Kaastra, Ciro Pinto, Liyi Gu, F. Mernier, Hong-Liang Yan, Yu-Ying Zhang and H. Akamatsu

Chemical abundances in the X-ray halos (also known as the intracluster medium, ICM) of clusters and groups of galaxies can be measured via prominent emission line features in their X-ray spectra. Elemental abundances are footprints of time-integrated yields of various stellar populations that have left their specific abundance patterns prior to and during the cluster and group evolution.We aim to constrain nitrogen abundances in the CHEmical Evolution RGS Sample (CHEERS), which contains 44 nearby groups and clusters of galaxies, in order to have a better understanding of their chemical enrichment. We examine the high-resolution spectra of the CHEERS sample carefully and take into account various systematic effects in the spectral modelling. We compare the observed abundance ratios with those in the Galactic stellar populations, as well as predictions from stellar yields (low- and intermediate-mass stars, massive stars and degenerate

This chapter has been submitted to Astronomy & Astrophysics, 2018

stars). The nitrogen abundance can only be well constrained ($\gtrsim 3\sigma$) in one cluster of galaxies and seven groups of galaxies. The [O/Fe] – [Fe/H] relation of the ICM is comparable to that for the Galaxy, while both [N/Fe] and [N/O] ratios of the ICM are higher than in the Galaxy. Future studies on nitrogen radial distributions are required to tell whether the obtained higher [N/Fe] and [N/O] ratios are biased due to the small extraction region ($r/r_{500} \lesssim 0.05$) that we adopt here. Since abundances of odd-Z elements are more sensitive to the initial metallicity of stellar populations, accurate abundance measurements of N, Na and Al are required to better constrain the chemical enrichment in the X-ray halos of clusters and groups of galaxies.

7.1. Introduction

Clusters of galaxies aggregate baryons and dark matter within large-scale structures that have collapsed under their own gravity. A large fraction (∼15−20%) of the total mass of a cluster is in the hot (T∼10^{7-8} K) X-ray halos (also known as the intracluster medium, ICM), while the member galaxies only make up for ∼3−5% of the total mass. The rest is in the form of dark matter. The ICM is an attractive laboratory for the study of nucleosynthesis and chemical enrichment (for a review, see Werner et al. 2008). Due to its deep gravitational potential well, a massive cluster ($M \gtrsim 10^{13}$ $M_\odot$, Renzini & Andreon 2014) can be considered as a "closed-box" (e.g. White et al. 1993), i.e. all the metals synthesized by different stellar populations in the member galaxies are conserved within the cluster. This assumption is based on the consistency (Landry et al. 2013) between the total cluster baryon fraction within a certain radius, say r_{500}[1], and the cosmic baryon fraction. This assumption does not necessarily hold for less massive groups of galaxies, due to the relatively shallow gravitational potential well. Once the metals are released via stellar winds, supernovae, etc., various metal transportation mechanisms working on different locations and time-scales distribute the metals into the X-ray halos. Relevant metal transportation mechanisms include Galactic winds, ram–pressure stripping, AGN–ICM interaction, and galaxy–galaxy interaction (for a review, see Schindler & Diaferio 2008).

Assuming that stellar populations where the metals are synthesized are representative, given stellar yields and observed abundance patterns in the X-ray halos,

[1]The radius within which the plasma mass density is 500 times the critical density of the Universe at the redshift of the groups and clusters of galaxies.

we are able to put constrains on the chemical enrichment to the largest gravitationally bound systems in the Universe (for a review, see Böhringer & Werner 2010). Given that α elements (e.g. O, Ne, Mg) are mainly produced in massive stars via core-collapse supernovae (SNcc), and Fe-peak elements are mainly produced in degenerate stars via Type Ia supernovae (SNIa), the SNIa fraction with respect to the total number of supernovae (SNcc plus SNIa) that enriched the ICM can be obtained by either fitting (e.g. de Plaa et al. 2006; Komiyama et al. 2009; Sanders & Fabian 2006; Sato et al. 2007; Werner et al. 2006b) the best-fit elemental abundances with supernova yields or applying directly supernova yields to immediately predict the X-ray spectrum (Bulbul et al. 2012). The latter assumes that the ICM can be described as a single temperature plasma in collisional ionized equilibrium (CIE). Unlike elements heavier than oxygen, carbon and nitrogen are mainly produced in low- and intermediate-mass stars (for a review, see Nomoto et al. 2013). Thus, the ICM abundances of C and N also provide important information to better understand the chemical enrichment.

Observationally, the abundances of α elements and Fe-peak elements can be measured with both low- and high-resolution grating spectra (e.g., de Plaa et al. 2017; Hitomi Collaboration et al. 2017a; Mernier et al. 2016a). Carbon and nitrogen abundances can only be determined from high-resolution grating spectra, such as those obtained with XMM–*Newton*/RGS (Reflection Grating Spectrometers, den Herder et al. 2001). Xu et al. (2002) first reported the nitrogen abundance in the hot X-ray halo of NGC 4636. Later, the nitrogen abundance was reported in other individual targets (Grange et al. 2011; Sanders et al. 2008, 2010; Tamura et al. 2003; Werner et al. 2006a, 2009) and in the stacked spectra of 62 groups and clusters of galaxies in Sanders et al. (2011).

In this work, we systematically study the nitrogen abundance in the CHEERS sample[2](de Plaa et al. 2017), which contains 44 nearby ($z < 0.1$) X-ray bright cool-core groups and clusters of galaxies. The key sample selection criterion (de Plaa et al. 2017) of the CHEERS sample is that the O VIII Lyα line at ~ 18.97 (rest frame) is detectable ($\gtrsim 5\sigma$) with RGS.

Throughout the paper we use $H_0 = 70$ km s^{-1} Mpc^{-1}, $\Omega_{\rm M} = 0.3$, $\Omega_\Lambda = 0.7$. For the spectral analysis (Section 7.3), we use C-statistics following Kaastra (2017). Unless specified otherwise, all errors correspond to the 68% confidence level for one interesting parameter.

[2]CHEERS is short for CHEmical Evolution Rgs cluster Sample.

7.2. Data reduction

We reduced both RGS and EPIC/MOS data following the same procedures described in Pinto et al. (2015), using XMM-*Newton* Science Analysis System[3] (SAS) v15.0.0. MOS data are reduced since the Reflection Grating Assemblies (RGAs) are aligned with the light path of the MOS cameras. We use MOS data for screening soft-proton flares and deriving the spatial extent of the source along the dispersion direction of RGS.

For each observation, we extract RGS spectra in a ∼3.4-arcmin-wide (along the cross-dispersion direction) region centred on the emission peak. This is done by setting the *xpsfincl* mask to include 99% of the line spread function (LSF) inside the spatial source extraction mask. The extraction region is somewhat different from the circular aperture used for the EPIC data analysis, especially when there is a gradient in temperature structure and/or metal abundances. The spectra and response matrices are converted to SPEX (Kaastra et al. 1996) format through the SPEX task *trafo*. The RGS modelled background spectra are subtracted.

The spatial extent along the dispersion direction of the source dominates the broadening of the emission lines, which can be described as (Tamura et al. 2004)

$$\Delta\lambda = \frac{0.138}{m}\frac{\Delta\theta}{\mathrm{arcmin}}, \tag{7.1}$$

where m is the spectral order, $\Delta\theta$ is the offset angle of the source. The average spatial extent of the ICM that includes half of the maximum line flux is ∼2′, that is to say, the average FWHM of the line profile (Equation 7.1) is ∼0.276 (1st-order) and ∼0.138 (2nd-order), respectively. The bin size that we used in our data processing with *rgsproc* is 0.01 (1st-order) and 0.005 (2nd-order), respectively. Hence we re-binned the RGS spectra by a factor of 10 for both 1st-order (7−28) and 2nd-order data (7−14), which approximately yielded the optimal binning (1/2−1/3 FWHM, Kaastra & Bleeker 2016) for RGS spectra of the ICM.

7.3. Spectral analysis

The high-resolution X-ray spectral analysis package SPEX (v3.03) is used to fit the RGS spectra. For collisional ionized equilibrium (CIE) plasma modelling, a large portion of the out-dated atomic data from the old version of SPEX (v.2.07) has been replaced with the state-of-the-art results published in the last decade, such

[3] http://www.cosmos.esa.int/web/*XMM-Newton*/sas

as level-resolved radiative recombination data (Badnell 2006; Mao & Kaastra 2016) and ionization balance that includes inner-shell ionization data (Urdampilleta et al. 2017). In addition, atomic data including collisional excitation/de-excitation rates, radiative transition probabilities and auto-ionization rates have been consistently calculated using the FAC[4] code (Gu 2008) and are included in the latest version of SPEX code as well. The *Hitomi* Soft X-ray Spectrometer (SXS) spectrum of the Perseus cluster offers an unprecedented benchmark of popular atomic codes, we refer to Hitomi Collaboration et al. (2017b) for more details.

For each cluster or group of galaxies, we fit simultaneously RGS1 and RGS2 spectra of each observation. Unless specified otherwise, the redshifts and Galactic absorption column densities are frozen to the values given in Pinto et al. (2015). We use the collisional ionization equilibrium absorption model (de Plaa et al. 2004; Steenbrugge et al. 2005) with a fixed temperature $T = 0.5$ eV to account for the Galactic neutral absorption. When modelling the thermal component(s) of the ICM, we consider three different differential emission measure (DEM) distributions.

1. The simplest scenario is assuming that the ICM is isothermal so that it can be described as a single temperature CIE model (denoted as 1T).

2. A more complicated scenario is that the ICM consists of a hotter and a cooler CIE component (denoted as 2T). Abundances of the two thermal components are assumed to be the same, while emission measures and temperatures are free to vary.

3. The most sophisticated scenario requires a multi-temperature DEM distribution. We adopted the GDEM model (de Plaa et al. 2006) here, which assumed a Gaussian distribution of the DEM in $\log\ T$,

$$Y(x) = \frac{Y_0}{\sigma\sqrt{2\pi}} \exp\left(-\frac{(x-x_0)^2}{2\sigma^2}\right), \tag{7.2}$$

where $x = \log(T)$ and $x_0 = \log(T_0)$, with T and T_0 (peak temperature of the distribution) in units of keV, and Y_0 is the emission measure. Apparently, when $\sigma = 0$, GDEM is identical to 1T. Again, abundances of the multi-temperature components are assumed to be the same.

The above three DEM distributions are driven by the results of Frank et al. (2013), where the authors measured $\mathrm{DEM} = dY/dT$ (where $Y = \int n_e n_H dV$ is the emission measure) distribution of 62 galaxy clusters in the HIFUGCS sample (Zhang

[4]https://www-amdis.iaea.org/FAC

et al. 2011). By comparing the goodness of the fit, one of the DEM distributions is favored and reported for each cluster or group. Regardless of the choice of the DEM distribution, the abundances of N, O, Ne, Mg, Fe, and Ni are free to vary, while the other elements heavier than He are frozen to 0.3 solar (e.g. Fujita et al. 2008; Werner et al. 2013). All the abundances are normalized to the proto-solar abundances of Lodders & Palme (2009), i.e. $z_{i,\,\mathrm{ICM}}/z_{i,\,\odot}$. The ionization balance described in Urdampilleta et al. (2017) is used. The spatial broadening is taken into account by convolving the thermal plasma model (1T/2T/GDEM) with the spatial broadening model (*lpro*).

The general strategy mentioned above does not necessarily provide an accurate measurement of elemental abundances. Special treatments are required in some cases. When $N_{\mathrm{H\ I}} \gtrsim 7 \times 10^{24}\ \mathrm{m}^{-2}$, the Galactic hydrogen column density (denoted as NH) is allowed to vary (de Plaa et al. 2017). When the ICM thermal emission is contaminated by non-thermal emission, a power law component is added accordingly with parameters fixed to literature values (e.g. for M 87 see Werner et al. 2006a). The derived abundance of a given element is proportional to the equivalent width, i.e. the ratio between the line flux and the continuum flux, given that the abundance is determined mainly from a well resolved emission line. That is to say, any uncertainty in the continuum would also impact the abundance measurement. When fitting the RGS spectra for a broad wavelength range (7–28 in our case), the continuum flux may be slightly over- or under-estimated due to uncertainties in the calibration of the RGS effective area, background subtraction, etc. Consequently, abundance measurement might be significantly biased, compared to the statistical uncertainties in the spectral fit. The same issue has been pointed out by Mernier et al. (2015) for their EPIC spectral analysis. Here we also performed the local fit (± 1 around the line centre) to check whether the global continuum level is correct or not, if not, the local fit results are adopted. Other systematic uncertainties regarding the spatial broadening of the line (Appendix 7.B.2) and RGS background model (Appendix 7.B.3) can be found in the Appendix 7.B.

7.4. Results and comparison with literature values

Nitrogen abundance measurements are best done in plasma with lower temperature (Figure 7.11). Therefore, in the CHEERS sample, we found that the nitrogen abundance can merely be well constrained ($\gtrsim 3\sigma$) in the core ($r/r_{500} \lesssim 0.05$) of one cluster of galaxies (A 3526) and seven groups of galaxies (M 49, M 87, NGC 4636, NGC 4649, NGC 5044, NGC 5813, NGC 5846). For some of the lower temperature

sources (e.g., NGC 3411) in the CHEERS sample, more exposure time is required to better constrain the nitrogen abundance. Spectral fits near the N VII Lyα line for these eight targets are shown in Figure 7.1 and the same (global) fits to the $7-28$ Å wavelength range can be found in Figure 7.10. The abundances and abundance ratios are summarized in Table 7.1.

The O/Fe ratios in the above eight sources (with the extraction region of ~3.4 arcmin) are $\lesssim 1.3$. Some of our results differ from those reported in de Plaa et al. (2017) for the 0.8-arcmin-wide extraction region. This is mainly due to the strong temperature and abundance gradients (Mernier et al. 2017), if present.

The N/Fe ratios reported in Table 7.1 are $\gtrsim 1.4$ with larger scatter. Xu et al. (2002), Werner et al. (2006a, 2009) and Grange et al. (2011) also reported similar N/Fe ratio $\gtrsim 1.4$ with large scatter between individual targets. Tamura et al. (2003) reported a lower N/Fe ratio of $\sim (0.6 \pm 0.2)$ for NGC 5044. The N/Fe ratios for individual targets reported in Sanders et al. (2008, 2010) are (spectral fitting) model dependent, with both higher ($\gtrsim$1) and lower ($\lesssim$1) values.

The N/O ratios reported here are above zero at the $\gtrsim 2.5\sigma$ confidence level. Sanders et al. (2011) reported a N/O ratio of 4.0 ± 0.6 in the stacked spectra of 62 groups and clusters of galaxies. Note that the authors also point out that, among individual targets in their sample, the nitrogen abundances vary considerably.

We caution that the reported abundance ratios in the literature depend on the details of the spectral analysis and/or the adopted extraction region. As discussed in great detail (de Plaa et al. 2017) the O/Fe ratio can be biased up to 30% (in total) due to various kinds of systematic uncertainties, including the effect of spatial line broadening, the choice of the multi-temperature model, the influence of the assumed value of galactic hydrogen column density ($N_{\rm H}$). In addition, the background level around the N VII Lyα neighbourhood is rather high in many cases (Figure 7.1). But the N/Fe ratio is not affected by the uncertainties (a $\lesssim 10\%$ constant bias) in the RGS modelled background (Appendix 7.B.3). As we mentioned in Section 7.4, we perform local fit in some cases (e.g. M 87) to mitigate some systematic uncertainties. In short, the overall systematic uncertainties of the N/Fe ratio is expected to be within 30%.

In addition, Smith et al. (2009) reported $\rm N/Fe \lesssim 3$ after analyzing optical spectra of ~150 red-sequence galaxies over a wide mass range in the Coma cluster and the Shapley Supercluster. Johansson et al. (2012) found $\rm N/Fe \lesssim 3$ for ~4000 early-type galaxies in a narrow redshift bin $z \in (0.05,\ 0.06)$ observed with Sloan Digital Sky Survey (SDSS). In contrast, Greene et al. (2015) measured a remarkably super-

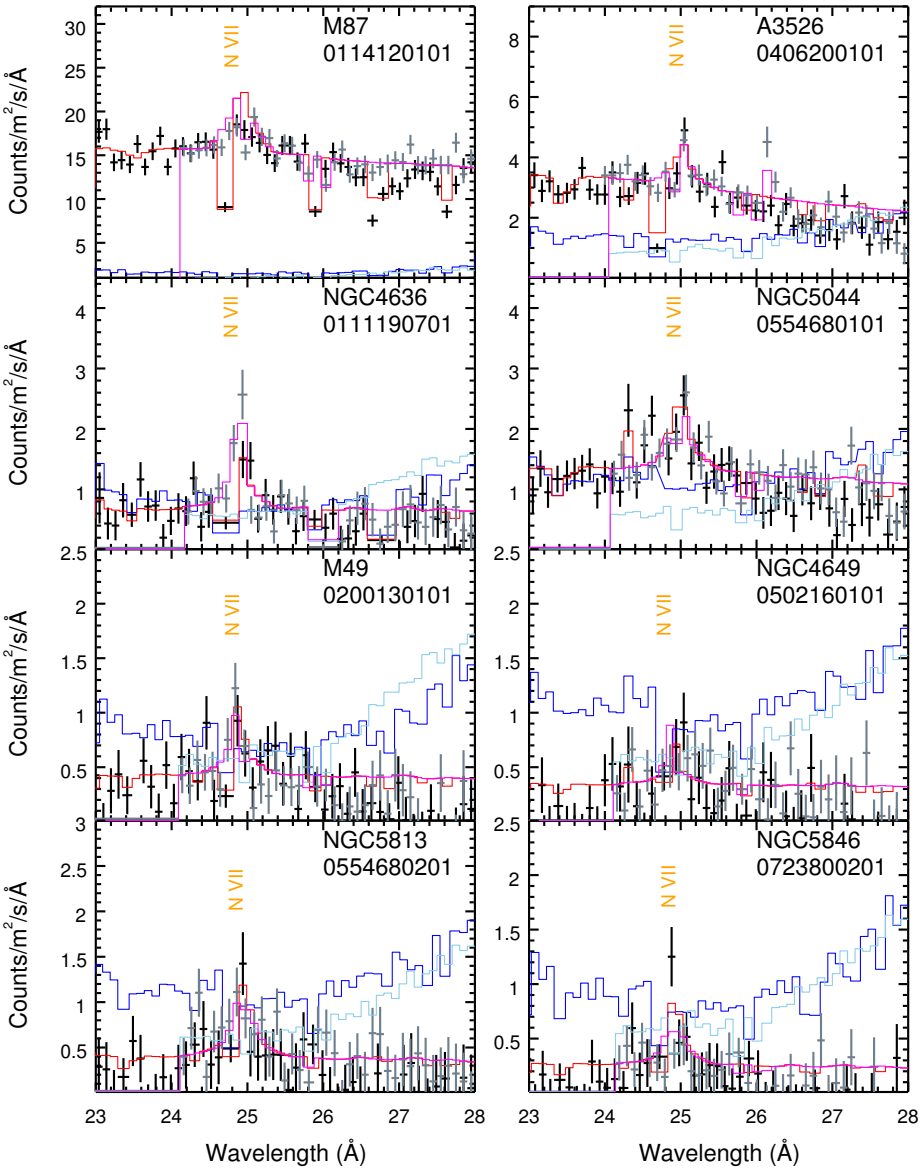

Figure 7.1: The global fits in the 18–28 wavelength range. The data points are shown in black (RGS1) and grey (RGS2), the modelled background spectra are shown in deep blue (RGS1) and light blue (RGS2) histograms, and the model spectra are shown in red (RGS1) and magenta (RGS2) histograms. Vertical dashed lines indicate the O VIII Lyα around 19 Å and N VII Lyα around 25 Å in the observed frame. Spectra from merely one observation per target are shown for clarity. Note that in the global fit to M 87 (the top-left panel), the N abundance is clearly overestimated, thus a local fit is performed (Section 7.4).

Table 7.1: Abundances and abundance ratios within the 3.4-arcmin-wide (along cross dispersion direction) extraction region.

Source	A3526	M49	M87	NGC4636	NGC4649	NGC5044	NGC5813	NGC5846
r/r_{500}	0.026	0.018	0.012	0.022	0.015	0.034	0.031	0.036
kpc	43.2	18.7	17.7	15.6	15.6	37.7	26.9	25.8
Model	NH+2T	GDEM	2T+PL	2T	1T	GDEM	2T	2T
C-stat./d.o.f.	2186/1088	852/544	3954/1111	748/480	1530/1096	1670/1094	2480/1649	1825/1093
$\sigma_{\mathrm{N/Fe}}$	$\sim 7\sigma$	$\sim 3\sigma$	$\sim 9\sigma$	$\sim 4\sigma$	$\sim 3\sigma$	$\sim 5\sigma$	$\sim 5\sigma$	$\sim 3\sigma$
N/O	2.7 ± 0.5	2.7 ± 1.0	2.2 ± 0.3	3.3 ± 1.1	2.9 ± 1.0	2.2 ± 0.5	3.2 ± 0.9	2.7 ± 0.8
N/Fe	1.5 ± 0.2	1.6 ± 0.6	1.8 ± 0.2	1.9 ± 0.5	2.4 ± 0.8	1.4 ± 0.3	1.9 ± 0.4	2.3 ± 0.7
O/Fe	0.54 ± 0.04	0.59 ± 0.10	0.82 ± 0.03	0.59 ± 0.08	0.84 ± 0.11	0.65 ± 0.05	0.58 ± 0.07	0.86 ± 0.12
Ne/Fe	0.57 ± 0.06	0.66 ± 0.17	0.55 ± 0.05	0.64 ± 0.12	1.07 ± 0.19	0.68 ± 0.08	0.53 ± 0.09	0.71 ± 0.14
Mg/Fe	0.66 ± 0.07	0.79 ± 0.19	0.24 ± 0.04	0.64 ± 0.13	1.40 ± 0.23	0.77 ± 0.08	0.83 ± 0.11	0.66 ± 0.14
Fe	1.02 ± 0.03	1.50 ± 0.12	0.55 ± 0.01	0.66 ± 0.04	0.55 ± 0.03	0.78 ± 0.03	0.92 ± 0.04	0.77 ± 0.05
Ni/Fe	1.2 ± 0.1	1.8 ± 0.5	0.65 ± 0.07	2.0 ± 0.4	2.5 ± 0.4	1.5 ± 0.3	$--$	2.0 ± 0.4

Notes. Abundances and abundance ratios are given according to the proto-solar abundance of Lodders & Palme (2009). $\sigma_{\mathrm{N/Fe}}$ is the significance level of nitrogen detection according to the N/Fe ratio (to be greater than zero). The uncertainties shown are 1σ statistical error bars. 1T, 2T and GDEM refer to single-temperature, two-temperature and multi-temperature differential emission measure (DEM) distribution (Section 7.3). For A 3526, "NH" refers to a free Galactic hydrogen column density in the spectral analysis. The Galactic hydrogen column densities for the other seven systems are frozen to literature values. For M 87, we use a power-law (PL) to model the non-thermal component, which is variable between the two observations (Werner et al. 2006a). For NGC 5813, Ni abundance cannot be constrained, and we fix it to solar during the fitting.

solar (at least three times solar) N/Fe abundance within a radius of 15 kpc for ~100 massive early-type galaxies. As pointed out by Greene et al. (2015), their N/Fe ratio would be three times solar if the O/Fe ratio were solar. In their default analysis, Greene et al. assume [O/Fe]=0.5, which leads to even higher N/Fe ratio. This assumed value of [O/Fe] is higher (by 0.2 dex or so) than some chemical enrichment model predicted (Nomoto et al. 2013; Pipino et al. 2009). A full spectral modelling is required to mitigate the impacts of blending and the uncertainties introduced by oxygen (Greene et al. 2015). Anyway, the O/Fe ratio assumed/predicted in the optical analysis is higher than that observed in the X-ray wavelength range. But it is possible that the SNcc products are preferably locked up by stars (Loewenstein 2013). In short, it is not trivial to compare and interpret the abundance ratios measured in the X-ray wavelength range and the optical wavelength range.

Moreover, The Ni/Fe abundance ratios reported in Table 7.1 differ from the solar Ni/Fe ratio found in the Perseus cluster (Hitomi Collaboration et al. 2017a). This might be due to the fact that the present work uses the L-shell lines which have large uncertainties in the current atomic codes.

7.5. Discussion

In the Galactic chemical evolution model (e.g. Kobayashi et al. 2006; Nomoto et al. 2013), nitrogen is mainly enriched via stellar winds of low- and intermediate-mass stars in the asymptotic giant branch (AGB). Therefore, in this section, we include the AGB enrichment channel (Section 7.5.1) for the chemical enrichment theory (e.g. Loewenstein 2013). We then compare the [O/Fe] – [Fe/H][5] and [N/Fe] – [Fe/H] relation between the ICM and different Galactic stellar populations, as well as the [N/O] – [O/Fe] relation between the ICM and supernova yields (Section 7.5.2). These comparisons enable us to discuss whether the nitrogen enrichment in the ICM shares the same origin as that in the Galaxy. Finally, we study elemental abundances in NGC 5044 (Section 7.5.3) to illustrate that by including odd-Z elements like nitrogen, the initial metallicity of the stellar population that enriched the ICM can be better constrained.

7.5.1. ICM Chemical enrichment

To interpret the observed time-integrated chemical abundances, we assume a single population of stars formed at high redshift (say, $z = 2 - 3$, Henriques et al. 2015)

[5] $[\mathrm{A/B}]_{\mathrm{ICM/star}} = \log_{10}\left(\frac{N_\mathrm{A}}{N_\mathrm{B}}\right)_{\mathrm{ICM/star}} - \log_{10}\left(\frac{N_\mathrm{A}}{N_\mathrm{B}}\right)_{\odot} = \log_{10}\left(\frac{Z_\mathrm{A}}{Z_\mathrm{B}}\right)_{\mathrm{ICM/star}}$.

with a common initial mass function (IMF). The ICM elemental abundance (the number of atoms of the ith element relative to that of hydrogen) relative to solar is defined as

$$Z_{i,\ \mathrm{ICM}} = \frac{z_{i,\ \mathrm{ICM}}}{z_{i,\ \odot}} = \frac{N^{\mathrm{li}}_{\mathrm{ICM}} < y^{\mathrm{li}}_{i} > + N^{\mathrm{m}}_{\mathrm{ICM}} < y^{\mathrm{m}}_{i} > + N^{\mathrm{d}}_{\mathrm{ICM}} y^{\mathrm{d}}_{i}}{M_{\mathrm{ICM}} X (A_i/A_H)(n_{i,\ \odot}/n_{\mathrm{H},\ \odot})}\ , \tag{7.3}$$

where $N^{li/m/d}_{\mathrm{ICM}}$ are the total number of low- and intermediate-mass stars (denoted with superscript "li") that enrich the ICM via the AGB channel, massive stars ("m") that explode as SNcc or PISNe (pair-instability supernovae), and single/double degenerate ("d") stars that explode as SNIa to enrich the ICM, $y^{\mathrm{li/m/d}}$ the corresponding stellar yields, M_{ICM} the mass of the ICM, A_i the atomic weight of the ith element, $A_{\mathrm{H}} = 1.0086\ a.m.u.$ the atomic weight of H, $n_{i,\odot}$ the elemental abundance by number in the solar abundance table and X is the mass fraction of H in the present universe.

The first two terms in the numerator of Equation (7.3) include the IMF weighted yields of low- and intermediate-mass or massive stars

$$< y_i >= \frac{\int_{m_{\mathrm{lo}}}^{m_{\mathrm{up}}} \phi(m) y_i(m) dm}{\int_{m_{\mathrm{lo}}}^{m_{\mathrm{up}}} \phi(m) dm}\ , \tag{7.4}$$

where $\phi(m)$ is the IMF, m_{lo} and m_{lo} the lower and upper mass limit (Z_{init} dependent, Table 7.2) of low- and intermediate-mass or massive stars considered.

It is unclear whether a universal IMF is applicable to all the clusters and groups of galaxies, or that the IMF depends on the local star formation rate (SFR) and/or metallicity of the environment (Mollá et al. 2015). For simplicity, other than the standard Salpeter IMF, we consider a top-heavy IMF, which is probably more relevant here, with an arbitrary IMF index (unity here). We caution that changing the IMF has profound consequences (Pols et al. 2012; Romano et al. 2005), including observables other than the chemical abundances that we measured here. For instance, a top-heavy IMF might make the galaxies too red (Saro et al. 2006). The global impacts on other observables introduced by the non-standard IMF are beyond the scope of this paper.

Additionally, the IMF weighted yield for massive stars, y^{m}_{i}, depends on the type(s) of supernovae that are taken into account for massive stars. We consider massive stars with stellar mass between 10 $M_{\odot}$ and 40 $M_{\odot}$ ($Z_{\mathrm{init}} > 0$) or 140 $M_{\odot}$ ($Z_{\mathrm{init}} = 0$) that undergo Fe core collapse at the end of their evolution and become

Table 7.2: The mass ranges (in $M_\odot$) used for calculating the IMF-weighted yields (Equation 7.4). For both low/intermediate-mass stars ("li", progenitors of AGBs) and massive stars ("m", progenitors of SNcc and PISNe), the mass ranges depend on the initial metallicity ($Z_{\rm init}$) of the stellar population.

$Z_{\rm init}$	$(m_{\rm lo},\ m_{\rm up})^{\rm li}$	$(m_{\rm lo},\ m_{\rm up})^{\rm m}$
0	(0.9, 3.5)	(11, 300)
0.001	(0.9, 6.5)	(13, 40)
0.004	(0.9, 6.5)	(13, 40)
0.008	(0.9, 6.5)	(13, 40)
0.02	(0.9, 7.0)	(13, 40)
0.05	(0.9, 7.0)	(13, 40)

Notes. The upper mass limit of intermediate-mass stars, defined as the minimum mass for the off-centre carbon ignition to occur, is smaller for lower metallicity (Gil-Pons et al. 2007; Siess 2007; Umeda & Nomoto 2002). The upper mass limit of massive stars depends on the types of supernovae that are taken into account. Massive stars that explode as core-collapse supernovae (with $m_{\rm up} = 40\ M_\odot$ for $Z \neq 0$ and an explosion energy of 10^{44} J) and pair-instability supernovae (with $m_{\rm up} = 300\ M_\odot$ and an explosion energy greater than 10^{44} J) are considered here.

Type II and Ib/c supernovae (i.e. core-collapse supernovae). Massive stars in the mass range of 25 $M_\odot$ to 40 $M_\odot$ ($Z_{\rm init} > 0$) or 140 $M_\odot$ ($Z_{\rm init} = 0$) can alternatively give rise to hypernovae (HNe) or faint supernovae (FSNe), instead of normal SNcc. Since the ratios among normal SNcc, HNe and FSNe for the relevant mass range are unknown for clusters and groups of galaxies, we do not consider HNe and FSNe enrichment for simplicity. In addition, we also take into account pair-instability supernovae (Umeda & Nomoto 2002) for zero initial metallicity ($Z_{\rm init} = 0$) enrichment, assuming that all the very massive stars, with stellar mass between 140 $M_\odot$ and 300 $M_\odot$, undergo pair-instability supernovae[6] (PISNe). Therefore, our calculation of the predicted abundance (Equation 7.3) is a first-order approximation.

The last term in the numerator of Equation (7.3) include $y_i^{\rm d}$, which is the yield per SNIa, and depends on the SNIa model. SNIa yields from Iwamoto et al. (1999), Badenes et al. (2006) and Maeda et al. (2010) are used for the following analysis.

In Table 7.3, we summarize the 12 sets of IMF weighted yields for non-degenerate stars that enrich the ICM via AGBs, SNcc (and PISNe). In Table 7.4 we summarize the 16 sets of SNIa yields for degenerate stars that enrich the ICM via SNIa.

Since measurement of the elemental abundances relative to hydrogen are limited to various uncertainties in the RGS spectral analysis (Appendix 7.B), the number of stars ($N_{\rm ICM}^{li/m/d}$ in Equation 7.3) in different enrichment channels (AGBs, SNcc and

[6] If very massive stars do not lose much mass, they are completely disrupted without forming a black hole via pair-instability supernovae (Barkat et al. 1967).

Table 7.3: Summary of the underlying model dependency for IMF power-law index and initial metallicity ($Z_{\rm init}$) of the stellar population (Equation 7.4).

Index	(IMF, $Z_{\rm init}$)	Index	(IMF, $Z_{\rm init}$)
1	(2.35, 0.0)	7	(1.0, 0.0)
2	(2.35, 0.001)	8	(1.0, 0.001)
3	(2.35, 0.004)	9	(1.0, 0.004)
4	(2.35, 0.008)	10	(1.0, 0.008)
5	(2.35, 0.02)	11	(1.0, 0.02)
6	(2.35, 0.05)	12	(1.0, 0.05)

Table 7.4: Summary of the underlying model dependency for SNIa enrichment (Equation 7.3).

Index	Model	Index	Model
1	CDD1	2	CDD2
3	W7	4	W70
5	WDD1	6	WDD2
7	WDD3	8	DDTa
9	DDTb	10	DDTc
11	DDTd	12	DDTe
13	DDTf	14	CDEF
15	ODDT	16	CDDT

Notes. [a] The IMF power-law index and the initial metallicity ($Z_{\rm init}$) of the stellar population. [b] SNIa models. The CDD (i.e. index 1 and 2) and WDD (5 to 7) models are delayed-detonation scenario (Iwamoto et al. 1999). The W (3 and 4) models refer to convection deflagration scenario (Iwamoto et al. 1999). The DDT (8 to 12) models are based on observational results from the Tycho supernova remnant (Badenes et al. 2006). The CDEF model refers to 2D deflagration scenario while both ODDT and CDDT models refer to 2D delayed-detonation scenario (Maeda et al. 2010).

SNIa) are not well constrained. Thus, we turn to the abundance ratios (relative to Fe), which can be better constrained. The abundance ratios in the ICM can be characterized by

$$\frac{z_{i,\,\mathrm{ICM}}}{z_{k,\,\mathrm{ICM}}} = \frac{r^{\mathrm{li}}_{\mathrm{ICM}} < y^{\mathrm{li}}_{i} > + < y^{\mathrm{m}}_{i} > + r^{\mathrm{d}}_{\mathrm{ICM}} y^{\mathrm{d}}_{i}}{r^{\mathrm{li}}_{\mathrm{ICM}} < y^{\mathrm{li}}_{k} > + < y^{\mathrm{m}}_{k} > + r^{\mathrm{d}}_{\mathrm{ICM}} y^{\mathrm{d}}_{k}} \frac{A_k\ n_{k,\,\mathrm{ICM}}}{A_i\ n_{i,\,\mathrm{ICM}}}\ , \tag{7.5}$$

where k is the reference atom number (specifically refers to Fe $Z = 26$ hereafter) and $r^{\mathrm{li/d}}_{\mathrm{ICM}} = N^{\mathrm{li/d}}_{\mathrm{ICM}} / N^{\mathrm{m}}_{\mathrm{ICM}}$.

7.5.2. Origin of nitrogen enrichment

We first compare the abundance relations between the ICM and the Galaxy. Figure 7.2 and Figure 7.3 show the [O/Fe] – [Fe/H] and [N/Fe] – [Fe/H] relations, respectively. The corrections for non-local thermodynamic equilibrium (NLTE) and three dimensional (3D) stellar atmosphere models are not taken into account for some N and O abundances in the metal-poor halo stars ([Fe/H]$\lesssim -1$) in Israelian et al. (2004) and Spite et al. (2005). Detailed NLTE and 3D corrections (see e.g. Asplund 2005, for a review), are beyond the scope of this paper and do not alter our interpretation below.

For the [O/Fe] – [Fe/H] relation (Figure 7.2), a gradual decrease of [O/Fe] with increasing [Fe/H] is found in the [Fe/H]$\lesssim -1$ regime. This is due to the fact that the more metal-poor the SNcc progenitor is, the larger the [O/Fe] ratio in the SNcc yields (Romano et al. 2010). The rapid decrease of [O/Fe] in the [Fe/H]$\gtrsim -1$ regime, on the other hand, stems from the Fe enrichment by SNIa. The [O/Fe] ratio of the ICM is slightly smaller compared to disc stars in the Galaxy with the same [Fe/H] ratio. The overall [O/Fe]–[Fe/H] relation of the ICM and the Galaxy still supports the idea that they share the same enrichment channel (SNcc plus SNIa) for O and Fe.

In contrast to the decreasing trend of [O/Fe] with increasing [Fe/H], a relatively flat [N/Fe] ratio with increasing [Fe/H] is found in Figure 7.3, which indicates that N and O are enriched via different channels. In fact, the [N/Fe] – [Fe/H] relation for the disk and halo stars can be explained (see Fig.3 in Romano et al. 2010) with AGB yields from Karakas (2010). The [N/Fe] ratio of the ICM is slightly larger compared to halo stars in the Galaxy with the same [Fe/H] ratio. The overall [N/Fe]–[Fe/H] relation of the ICM and the Galaxy indicates that they share the same enrichment channel (AGB) for N.

Secondly, we compare the [N/O]–[O/Fe] relation of supernova yields (Figure 7.4)

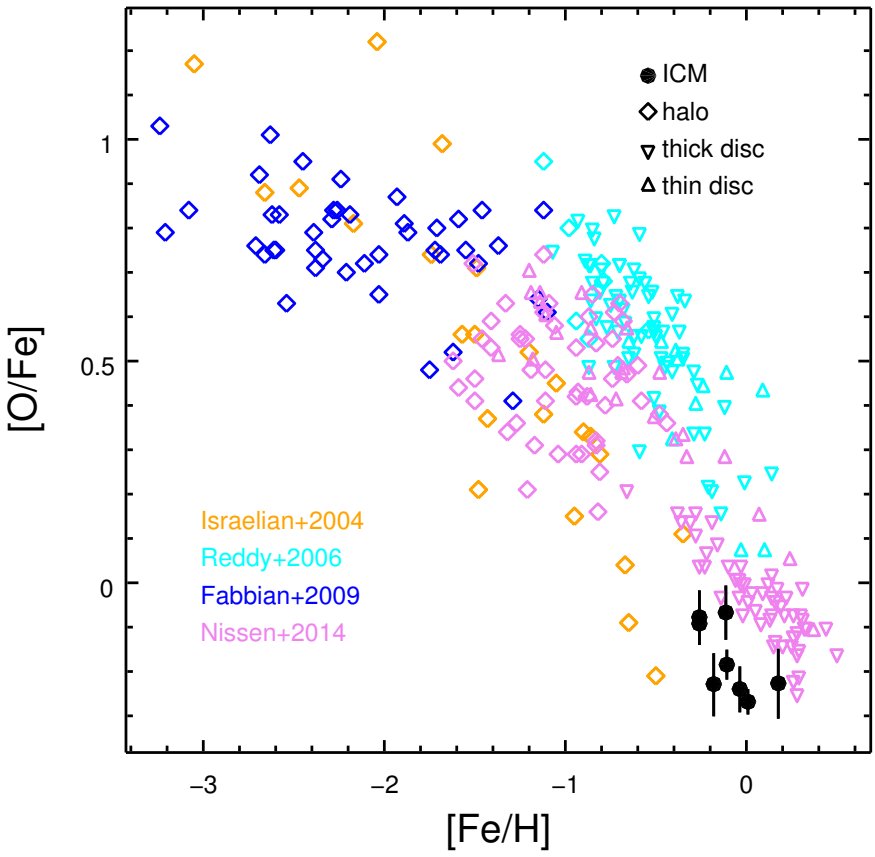

Figure 7.2: The [O/Fe] – [Fe/H] relation for ICM and the Galaxy. The ICM Fe abundances and O/Fe abundance ratios (Table 7.1) are shown as black dots with (statistical) error bars.The Galactic Fe abundances and O/Fe abundance ratios are taken from Israelian et al. (2004) (halo, orange), Reddy et al. (2006) (disc and halo, cyan), Fabbian et al. (2009) (halo, blue) and Nissen et al. (2014) (disc and halo, pink).

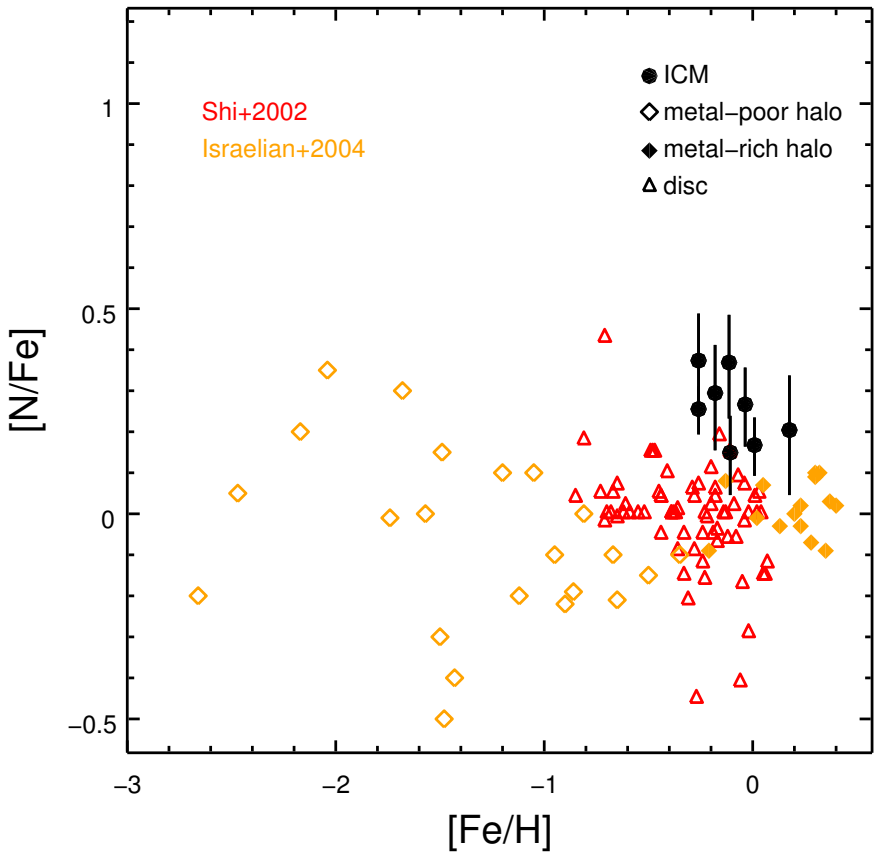

Figure 7.3: Similar to Figure 7.2 but for the [N/Fe] – [Fe/H] relation. The Galactic Fe abundances and N/Fe abundance ratios are taken from Shi et al. (2002) (disc, red triangles) and Israelian et al. (2004) (halo, orange diamonds).

to the observed abundances (Figure 7.5). The [O/Fe] ratio of the ICM is smaller compared to that of halo stars since the ICM is enriched by both SNcc and SNIa, while halo stars are mainly enriched by SNcc. Generally speaking, the [N/O] ratio in the ICM is larger than that of halo stars. Similar results have been reported in Werner et al. (2006a) for M 87.

If the chemical enrichment were completely due to massive stars ($N_{\rm ICM}^{\rm li/d} = 0$ in Equation 7.3), then we would have [O/Fe]$\gtrsim 0.5$ (Figure 7.4), except for $Z_{\rm init} = 0$. For $Z_{\rm init} = 0$, the [O/Fe] ratio can be lower than ~0.5, due to the explosive O-burning by PISNe (Nomoto et al. 2013). In Figure 7.4, we assume all the very massive stars undergo PISNe (Section 7.5.1). In reality, the exact value of [O/Fe] (for $Z_{\rm init} = 0$) might differ, depending on the IMF and the fraction of very massive stars that undergo PISNe. The [O/Fe] ratios in the ICM (Figure 7.5) are in the range of (-0.5, 0.2), suggesting that the enrichment from SNIa is required for the ICM, unless PISNe contributes significantly.

The nitrogen enrichment via SNIa is negligible ([N/O]$\lesssim -1$). Therefore, one would expect [N/O] $\lesssim -0.2$ (Figure 7.4), if the chemical enrichment were completely due to massive stars ($N_{\rm ICM}^{\rm li/d} = 0$ in Equation 7.3). We caution that the [N/O] ratio for $Z_{\rm init} = 0$ in Figure 7.4 is in fact a lower limit, since we do not include enrichment from metal-poor rotating massive stars before they explode as supernovae which is due to the lack of knowledge of corresponding number fraction and yields. Chiappini et al. (2006) have shown that a contribution, as large as [N/Fe]~0.5, from metal-poor ([Fe/H] $\lesssim$-2.5) rotating massive stars is required to solve the primary nitrogen problem (see also Fig.3 in Romano et al. 2010). For a Salpeter IMF, the upper limit of [N/O] is estimated to be zero, given that not all the metal-poor massive stars are rotating (thus [N/Fe] $\lesssim 0.5$) and [O/Fe]$\gtrsim 0.5$ (Figure 7.4), regardless of $Z_{\rm init}$. The same upper limit of [N/O] holds for a top-heavy IMF with $Z_{\rm init} \gtrsim 0.001$. Nonetheless, for a top-heavy IMF with $Z_{\rm init} \lesssim 0.001$, the upper limit of [N/O] might be above zero, since [O/Fe] ratio can be lower than 0.5 as previously discussed.

The [N/O] ratios in the ICM are above zero at the $\gtrsim 2.5\sigma$ confidence level (Table 7.1), indicating that under a Salpeter IMF, the massive stars cannot be the main nitrogen factory. In this case, nitrogen mainly originates from low- and intermediate-mass stars (AGBs). Nevertheless, we cannot rule out that under a top-heavy IMF with a low initial metallicity ($Z_{\rm init} \lesssim 0.001$), massive stars could be an important nitrogen enrichment factory.

Last but not least, we caution that the measured [N/Fe] and [N/O] ratios in Table 7.1 might be biased. Due to the limited field of view (FOV) of RGS, the

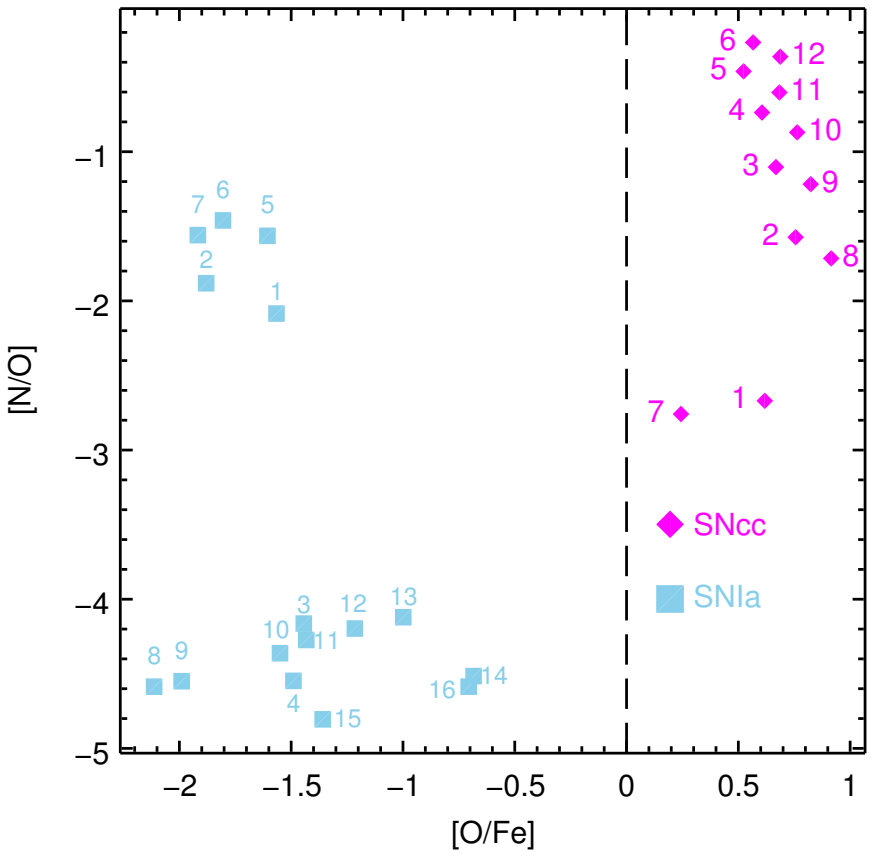

Figure 7.4: The diamonds (magenta) are the IMF-weighted yields of SNcc (and PISNe for $Z_{\rm init} = 0$), while the squares (blue) are SNIa yields. The indices next to the symbols indicate corresponding model dependency (Tabel 7.3 and Tabel 7.4). The yields of all the elements from C to Zn can be found in Figure 7.15 and 7.16.

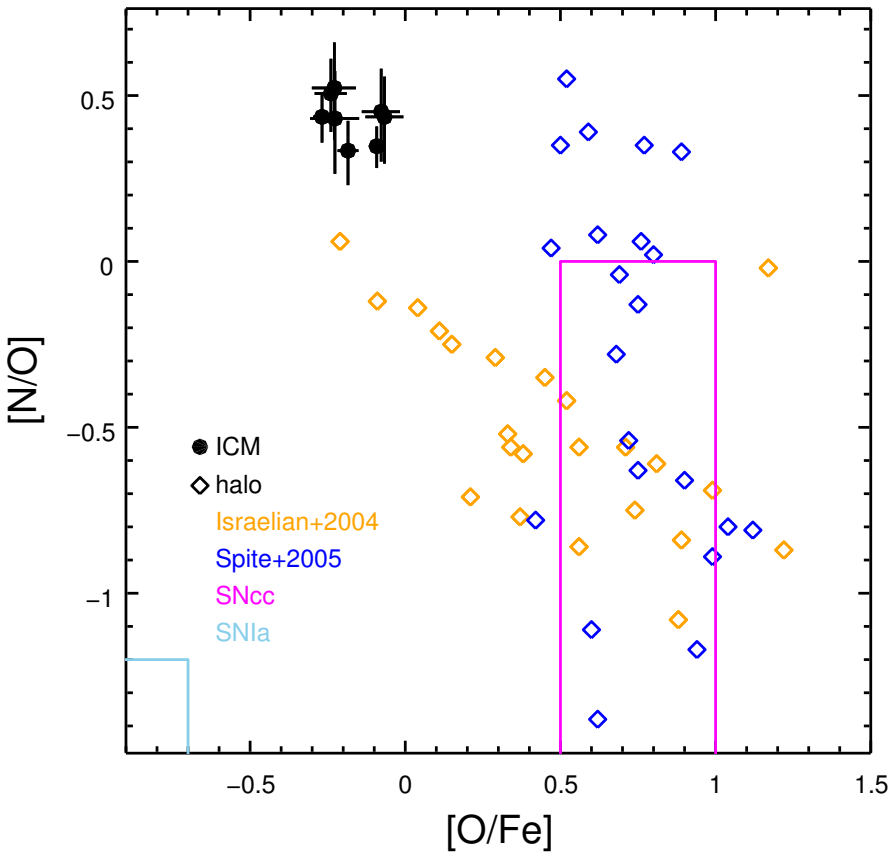

Figure 7.5: Similar to Figure 7.2 but for [N/O] vs. [O/Fe].The results for Galactic stellar populations are taken from Israelian et al. (2004); Spite et al. (2005) (halo, diamonds). The magenta box indicates the region of SNcc yields except for $Z_{\rm init} = 0$, while the blue box indicates the region of SNIa yields (Figure 7.4).

abundance ratios obtained in the rather small ($\lesssim 0.05 r_{500}$) extraction regions do not necessarily represent the abundance patterns within the "closed-box" (Section 7.1). If the elements enriched via different channels were distributed into the ICM in different ways, so that, for instance, N were more centrally peaked than Fe and O, the resulting [N/Fe] and [N/O] ratios in the core region would appear to be larger.

7.5.3. Odd-Z elements

Previous studies on chemical enrichment in the ICM mainly focused on determining the SNIa fraction with respect to the total number of SNe that enriched the ICM (e.g. de Plaa et al. 2006). In terms of elemental abundances, most abundant even-Z elements from oxygen up to and including nickel (except Ti) have been measured. Additionally, one odd-Z Fe-peak element, Mn, is also studied in the stacked spectra of the CHEERS sample (Mernier et al. 2016a). In terms of yields table, in addition to SNcc and SNIa, Pop III stars (de Plaa et al. 2006; Werner et al. 2006b) and Ca-rich gap transients (CaRGT, Mulchaey et al. 2014) have also been taken into account to interpret the observed abundance pattern. In this section, we include the nitrogen abundance and yields from AGBs (Campbell & Lattanzio 2008; Karakas 2010; Nomoto et al. 2013) for the chemical enrichment study of the ICM.

Since the number of abundance ratios derived from the RGS spectra are rather limited, due to the relatively small coverage of the energy range, it is more meaningful when the abundance ratios measured with EPIC are also taken into account. Ideally, one needs to obtain the abundances within $\sim r_{500}$ of the ICM so that the "closed-box" assumption is valid for massive clusters (Section 7.1). In practice, especially for groups of galaxies, the FOV of RGS covers merely a tiny fraction of r_{500}. Moreover, the unknown nitrogen abundance gradients within r_{500}, prevent us from extrapolating the abundances out to r_{500} with the obtained RGS abundances by hand.

We use both the RGS and EPIC results of NGC 5044 (Table 7.5) for the exercise here, given that the measurement uncertainty of the nitrogen abundance is typical (neither too large nor too small), and the extraction regions are comparable ($\sim$0.034 r_{500} for RGS and $\sim$0.05 r_{500} for EPIC). In Table 7.5, the N/Fe, O/Fe, Ne/Fe, Mg/Fe, and Ni/Fe abundance ratios are measured with RGS, while the Si/Fe, S/Fe, Ar/Fe, and Ca/Fe ratios are measured with EPI (see details in Appendix 7.C).

We emphasize that we focus on the comparison among different settings of the ICM enrichment model, i.e. the choice of IMF index and the initial metallicity of the stellar population, the choice of SNIa model, and whether to include enrichment

Table 7.5: The abundance ratios for NGC 5044 within the extraction region (i.e. $\lesssim r/r_{500}$). Abundance ratios measured with EPIC spectra are labeled with †.

X/Fe	Value
N/Fe	1.4 ± 0.3
O/Fe	0.65 ± 0.05
Ne/Fe	0.68 ± 0.08
Mg/Fe	0.77 ± 0.08
Si/Fe†	0.79 ± 0.10
S/Fe†	1.1 ± 0.2
Ar/Fe†	1.0 ± 0.3
Ca/Fe†	1.2 ± 0.2
Fe	0.72 ± 0.02
Ni/Fe	1.5 ± 0.3

from AGBs or not.

It is possible that SNIa from different channels (via single- or double-degenerate, deflagration or detonation, and super- or sub-Chandrasekhar limit) all play a role in the chemical enrichment of the ICM (Finoguenov et al. 2002; Mernier et al. 2016b). We only fit the measured abundance ratios with one set of SNIa yields for simplicity. Including an additional set of Ca-rich gap transients yields improves the statistics negligibly and does not change the above main points.

Since almost all the measured abundance ratios (Table 7.5) are close to solar, we restrict the initial metallicity of stellar populations to be solar and sub-solar (i.e. excluding $Z_{\rm init} = 0.05$). Thus, the observed abundance ratios are fitted to 10 (2 sets of IMF and 5 sets of $Z_{\rm init}$) $\times$16 (for SNIa) combinations of yield tables. The reduced chi-squared ($\chi^2_{\rm red}$) for all the fits are shown in the upper panel of Figure 7.6. The 10×16 combinations of the chemical enrichment models are highly degenerate. We can reject a large number of combinations based on the statistics, say $\chi^2_{\rm red} \gtrsim 3$, i.e. $\log_{10}(\chi^2_{\rm red}) \gtrsim 0.5$, however, the IMF power-law index and SNIa models cannot be exclusively obtained with current abundance measurements.

Typical "best" fits of the abundance ratios in NGC 5044 to stellar yields are shown in Figure 7.7 (without the N/Fe ratio and yields from AGBs) and Figure 7.8 (with the N/Fe ratio and yields from AGBs). Without yields from AGBs (Figure 7.7), we also show the model prediction on the N/Fe ratio (~ 0.2). Compared to the measured N/Fe ratio (1.4 ± 0.3), the predicted N/Fe ratio is lower by $\sim 4\sigma$, indicating that the contribution from SNcc is not enough to explain the observed N/Fe ratio. When we include yields from AGBs (Figure 7.8), the predicted N/Fe ratio is consistent ($\lesssim 1\sigma$) with the observed N/Fe ratio. Additionally, the predicted O/Fe ratio decreases from

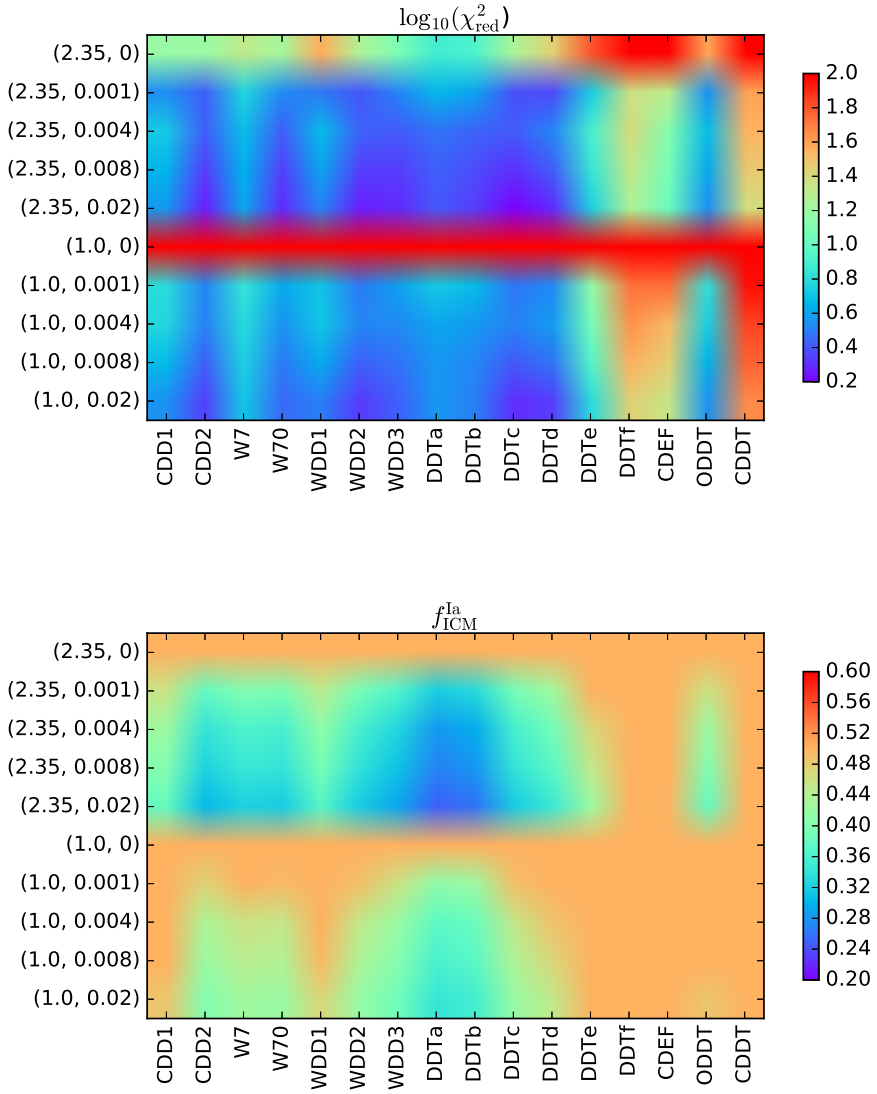

Figure 7.6: Color map of reduced chi-squared (χ^2/d.o.f. in $\log_{10}$-scale, upper panel) and SNIa fraction ($f^{\rm Ia}_{\rm ICM}$, lower panel) for 10×16 combinations of yields we considered to fit the abundance ratios in NGC5044, without N/Fe (d.o.f. = 7). The X-axis labels indicate the SNIa models. The Y-axis labels indicate IMF power-law index and the initial metallicity of the stellar populations.

~0.69 (SNe) to ~0.66 (SNe + AGBs) due to the negative oxygen yields in AGBs.

In most cases, a Salpeter IMF provides better χ^2 statistics (Figure 7.6). When a Salpeter IMF and DDTc SNIa model are adopted, the SNIa fraction ($f_{\rm ICM}^{\rm Ia}$) is consistent with $\sim 32\%$, whether we include N/Fe and AGBs enrichment or not (Figure 7.7 and 7.8). The ratio ($r_{\rm ICM}^{\rm li} = r^{\rm li}/r^{\rm m}$) between the number of low- and intermediate-mass stars and that of massive stars is 180 ± 50. Under a Salpeter IMF, the ratio ($r_{\rm ICM}^{\rm li}$) is expected to be ~ 40, which is lower than the fitted value by $\sim 3\sigma$. Again, the "closed-box" assumption is not fulfilled here, so that if the AGB products were more centrally peaked than the SNcc products (Section 7.5.2), a higher $r_{\rm ICM}^{\rm li}$ obtained here could be explained.

When N/Fe and AGB enrichment are not included in the fit, the "best" fit initial metallicity is 0.02 (solar). This is mainly constrained by the less than unity O/Mg abundance ratio (Figure 7.9). Including N/Fe and AGB enrichment again favours solar initial metallicity. We also notice that, in both cases, a wide range of $Z_{\rm init}$ yields comparable results (Table 7.6), except for $Z_{\rm init} = 0$.

In principle, when odd-Z elemental abundances, like nitrogen, are included in the analysis, the initial metallicity of the stellar population should be better constrained, since yields of odd-Z elements increase significantly with increasing $Z_{\rm init}$ owing to a surplus of neutrons (Nomoto et al. 2013), while those of even-Z and Fe-peak elements are almost constant over a wide range of metallicities. This is shown clearly in Figure 7.9 for massive stars. We emphasize that the denominator of the abundance ratio on the Y-axis is set to Mg instead of Fe in Figure 7.9. This is because Mg enrichment via SNIa and AGBs are negligible, so that the observed abundance ratios of Na/Mg and Al/Mg can be used directly to probe the initial metallicity of the stellar population.

For future work, more accurate abundance measurements of odd-Z elements including N, Na and/or Al are required to better constrain the initial metallicity of the stellar population. Current instruments lack the spectral resolution to resolve the Lyα lines of Na XI and Al XIII. Hopefully, future missions with high spectral resolution and large effective area like *XARM* (X-ray astronomy recovery mission) and *Athena* (Nandra et al. 2013) will address this issues.

7.6. Conclusions

We constrain the N/Fe ratio in the core ($r/r_{500} \lesssim 0.5$) of one cluster (A 3526) and seven groups of galaxies (M 49, M 87, NGC 4636, NGC 4649, NGC 5044, NGC 5813, NGC 5846) in the CHEERS sample with high-resolution RGS spectra. Our main con-

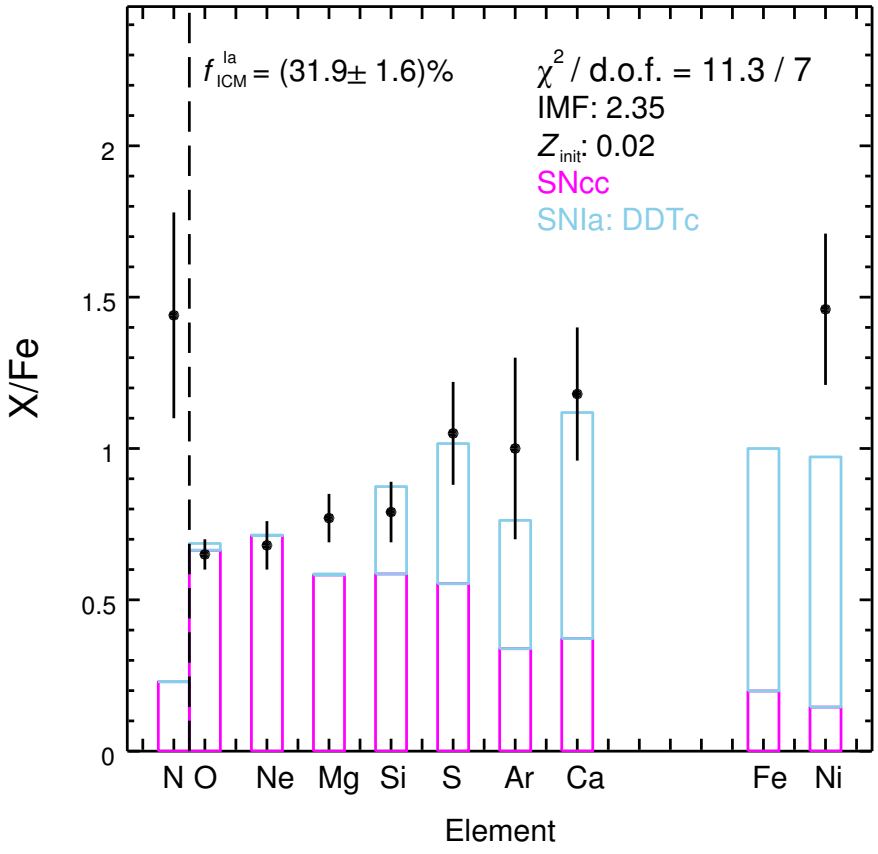

Figure 7.7: One of the acceptable fits of chemical enrichment in NGC 5044. Yields of SNcc (magenta) and SNIa (blue) are used for the fit with Equation (7.5). The adopted IMF power-law index is 2.35 (Salpeter) and the initial metallicity of the stellar population is 0.02 (solar). N/Fe and yields of AGBs are not included in the fit, but shown for comparison. The SNIa fraction $f_{\rm ICM}^{\rm Ia} = r^{\rm d}/(r^{\rm d}+1)$ is $(31.9\pm1.6)\%$.

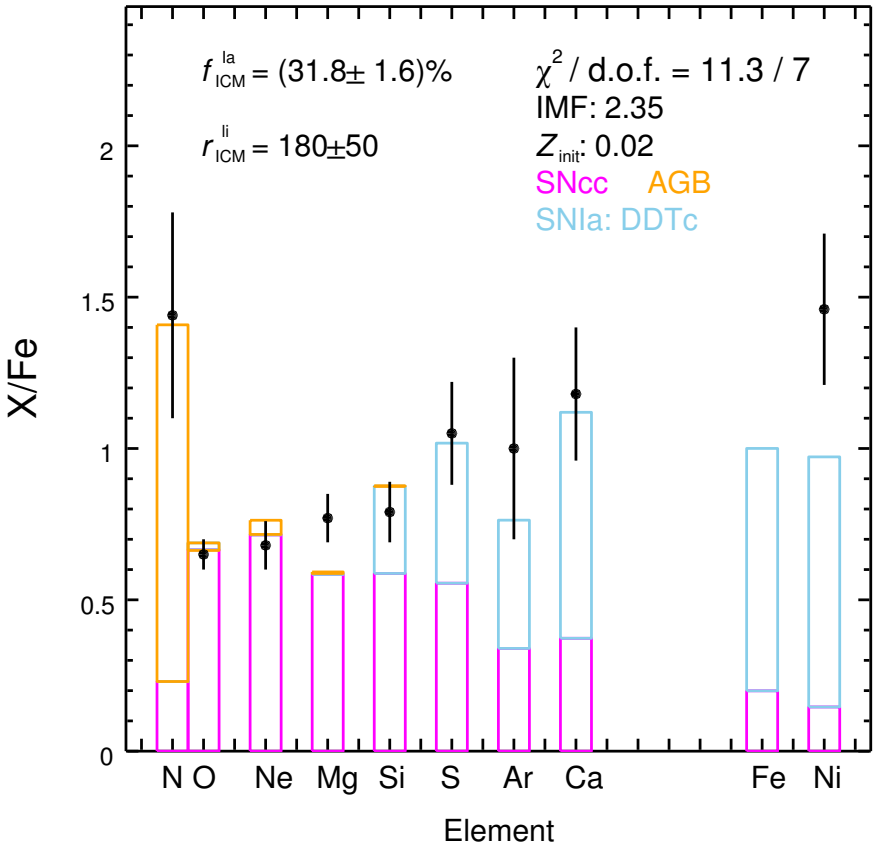

Figure 7.8: Similar to Figure 7.7 but N/Fe and AGB yields (orange) are included during the fit. Again, the favored IMF power-law index is 2.35 (Salpeter) and $Z_{\rm init} = 0.02$. The SNIa fraction is consistent with the previous result. The ratio ($r^{\rm li}_{\rm ICM} = r^{\rm li}/r^{\rm m}$) between the number of low- and intermediate-mass stars and that of massive stars is 180 ± 50.

Table 7.6: The "best" fits (d.o.f. = 7) of chemical enrichment in NGC 5044, given the IMF power-law index and initial metallicity of the stellar population.

IMF[a]	$Z^{b}_{\rm init}$	SNIa	AGB[c]	χ^2
2.35	0.02	DDTc	N	11.3
2.35	0.008	DDTc	N	14.5
2.35	0.004	WDD3	N	18.1
2.35	0.001	DDTd	N	16.5
2.35	0	DDTa	N	53.9
1.0	0.02	DDTc	N	14.2
1.0	0.008	DDTc	N	18.0
1.0	0.004	DDTc	N	22.7
1.0	0.001	DDTc	N	21.5
1.0	0	DDTa	N	>100
2.35	0.02	DDTc	Y	11.3
2.35	0.008	DDTc	Y	13.2
2.35	0.004	DDTc	Y	14.5
2.35	0.001	DDTd	Y	22.5
2.35	0	DDTa	Y	52.5
1.0	0.02	DDTc	Y	13.7
1.0	0.008	DDTc	Y	15.7
1.0	0.004	DDTc	Y	18.7
1.0	0.001	DDTc	Y	18.4
1.0	0	DDTa	Y	>100

Notes. [a] The power-law index of the IMF. [b] The initial metallicity of the stellar populations. [c] Whether the N/Fe ratio and the yields of AGBs are included in the fit.

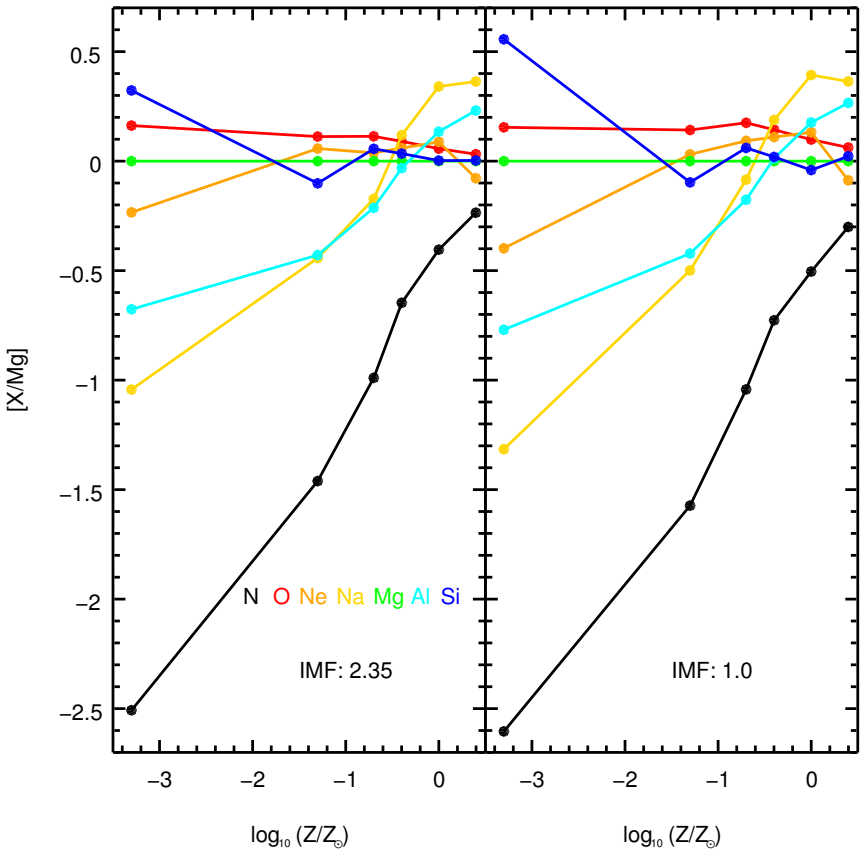

Figure 7.9: The IMF weighted abundance ratios (with respect to Mg) as a function of the initial metallicity of massive stars (the SNcc channel). The results for $Z_{\rm init} = 0$ are plotted at ~ -3.3.

clusions are summarized as follows:

1. The nitrogen abundance is well constrained ($\gtrsim 3\sigma$) in objects with a relatively cool ICM ($kT \lesssim 2$ keV). For some of the systems (e.g. NGC 3411) in the CHEERS sample, more exposure time is required to better constrain the nitrogen abundance. In objects with a hotter ICM ($kT \gtrsim 2-3$ keV), the continuum level is high so that weak emission lines like N VII Lyα cannot be well constrained.

2. Both the [O/Fe]–[Fe/H] and [N/Fe]–[Fe/H] relations observed in the ICM are comparable to those observed in different stellar populations in the Galaxy, indicating that the enrichment channels for N, O and Fe are expected to be the same. One possible explanation for the super solar N/Fe and N/O ratios in the ICM is the bias introduced by our small extraction region ($r < 0.05r_{500}$). This potential bias can be confirmed by radial abundance maps for N, O, and Fe in future work.

3. If the observed ratio [N/O]> 0 (at the $\gtrsim 2.5\sigma$ confidence level) is not biased due to the small extraction region, under a Salpeter IMF, the low- and intermediate-mass stars are found to be the main metal factory for nitrogen. This is in agreement with the Galactic chemical evolution theory and previous studies of M 87. Nitrogen enrichment from massive stars might still be important, especially if the stellar population would have a top-heavy IMF and zero initial metallicity.

4. We find the obtained SNIa fraction is insensitive to the N abundance and AGB yields.

5. We also point out that accurate abundance measurements of odd-Z, such as N, Na, and Al can certainly help to better constrain the initial metallicity of the stellar population that enriched the ICM.

7.A. Global spectral fit

The global fits to the 7–28 wavelength range for each source in Table 7.1 are shown in Figure 7.10. The location (in the observed frame) of characteristic emission lines are labeled, including the Lyα line from H-like N VII, O VIII, Ne X, Mg XII, He-like triplets from O VII, Ne IX, Mg XI and the resonance and forbidden lines of Ne-like Fe XVII.

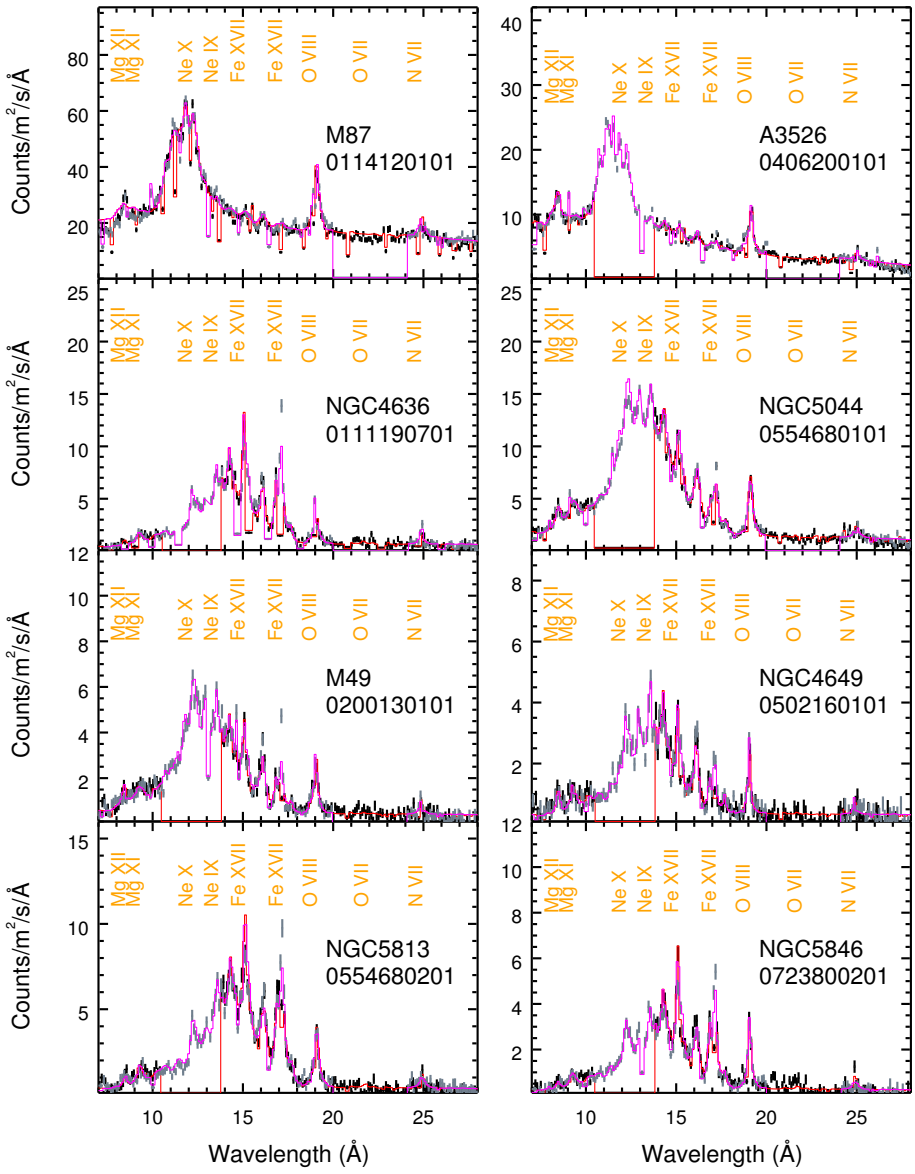

Figure 7.10: The global fits to the 7–28 wavelength range. The data points are shown in black (RGS1) and grey (RGS2) and the model spectra are shown in red (RGS1) and magenta (RGS2) histograms. Spectra from merely one observation per target are shown for clarity.

7.B. Systematic uncertainties in spectral analysis

7.B.1. Differential emission measure distribution

Fitting a multi-temperature plasma with a single temperature (1T) model would often over-estimate the emission measure and under-estimate the abundances (Buote 2000; Buote & Canizares 1994). Alternatively, a two-temperature (2T) or multi-temperature (GDEM) model can measure the nitrogen abundance more accurately.

In a 2T model, if the emission measure of the hotter component is $\gtrsim 5$ times that of the cooler one, the N VII in the hotter CIE component contributes more to the observed N VII Lyα emission in the spectra. Given the same emission measure and nitrogen abundance, the N VII Lyα line flux is proportional to the N VII ion concentration (relative to all the nitrogen atoms and ions in the ICM) times the level occupations of $^2P_{0.5}$ and $^2P_{1.5}$ (the sum of occupations of all the levels are defined as unity). As the level occupations increase gradually as a function of plasma temperature (bottom panel in Figure 7.11), the N VII ion concentration is the leading factor to determine the line emissivity. As mentioned above, we tie the abundances in our 2T model, thus, assuming $kT_{\rm c} \lesssim 0.7$ keV and $kT_{\rm h} \gtrsim 2$ keV, when $Y_{\rm c}/Y_{\rm h} \lesssim 0.2$, the N VII in the hotter component contributes more to the emission line, while for $Y_{\rm c}/Y_{\rm h} \gtrsim 0.2$, the N VII is mainly from the cooler component.

In addition, the line emissivity of N VII Lyα peaks around $T \sim 2\times10^6$ K (Kaastra et al. 2008), implying that nitrogen is preferably found in relatively cooler plasma. As the line emissivity declines rapidly with the increasing temperature of the plasma (top panel in Figure 7.11), we find it is rather difficult to well constrain the nitrogen abundance via the extremely weak N VII Lyα emission line embedded in the relatively high continuum where $kT \gtrsim 2-3$ keV.

7.B.2. Spatial broadening model

The spatial broadening model *lpro* is built based on the spatial broadening profile. The latter is obtained from the MOS1 image, since the MOS1 DETY direction is in parallel to the RGS1 dispersion direction. There are two more free parameters in *lpro*, the scaling factor (s) and the offset parameter. Here we discuss the systematic uncertainties of the spatial broadening model.

For instance, in M 87, due to the presence of the bright non-thermal emission in the second observation (ObsID: 0200920101), not only the spectra are heavily contaminated, but also the spatial broadening model created with the MOS1 image is affected. The brighter the central non-thermal emission, the more centrally peaked

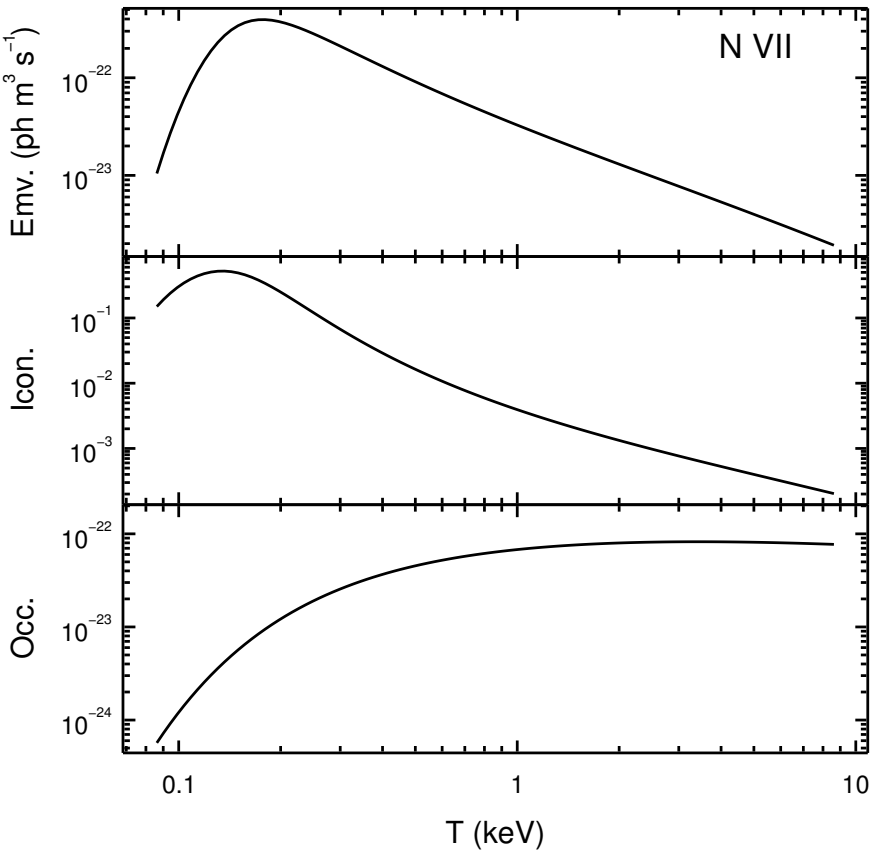

Figure 7.11: The N VII Lyα line emissivity (top), relative ion concentration (middle) and relative level occupation (bottom) of the two upper levels $^2P_{0.5}$ and $^2P_{1.5}$ (in sum, since the fine-structure lines cannot be distinguished). The underlying ionization balance is Urdampilleta et al. (2017) and the proto-solar abundance of Lodders & Palme (2009) is used. In a hot ($kT \gtrsim 0.6$ keV) single-temperature CIE plasma, nitrogen is almost fully ionized in the form of N VIII, i.e. the ion concentration of N VIII is ~ 1. Most of the N VII is in the ground level $^1S_{0.5}$, i.e. the level occupations of $^1S_{0.5}$ is close to unity.

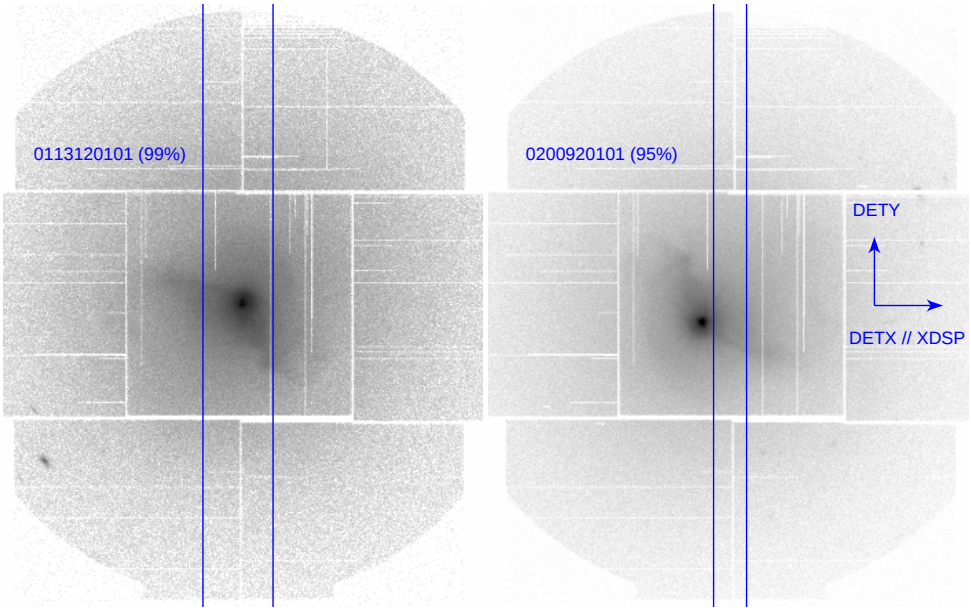

Figure 7.12: The 7–28 energy band MOS1 image in the detector coordinate system for M87. The MOS1 DETX axis is in parallel with the cross dispersion direction (XDSP) of RGS. In the second observation (0200920101), the non-thermal emission is much brighter, offset by ~1.5 arcmin and the image is rotated ~188 degrees clockwise. The (blue) rectangular boxes indicated the extraction regions for *rgsvprof*. For the first observation, a 99%-xpsf (~3.4 arcmin) extraction region, aligned with the RGS source extraction region, is used. For the seconding observation, only the onset 95%-xpsf (~1.6 arcmin) extraction region (to avoid central contamination) is shown for clarity.

the surface brightness profile (seen indirectly in Figure 7.13). Spatial broadening models built on these biased surface brightness profiles reflect no longer the proper spatial extent of the ICM.

We compare the (global) fit results using different line broadening profile of M 87 here. If the non-thermal emission were merely a point source and the ICM were azimuthally symmetric, one might fit the observed 2D image with two Gaussian/Lorentzian profiles with different widths, then subtract the non-thermal emission counterpart to obtain the profile for the ICM only. However, this is not the case for M 87 due to its azimuthal asymmetry (Figure 7.12). Because the emission centre is offset by ~1.5 arcmin in 0200920101, we took advantage of a ~1.6-arcmin-wide extraction region without the non-thermal emission, leading to a better yet still biased (probably flatter) spatial broadening model (Figure 7.13). Whereas, we found the *lpro* scaling factor (free parameter) can account for the bias in the spatial broadening profile.

Other than the accuracy of the spatial broadening profile, the scaling factors

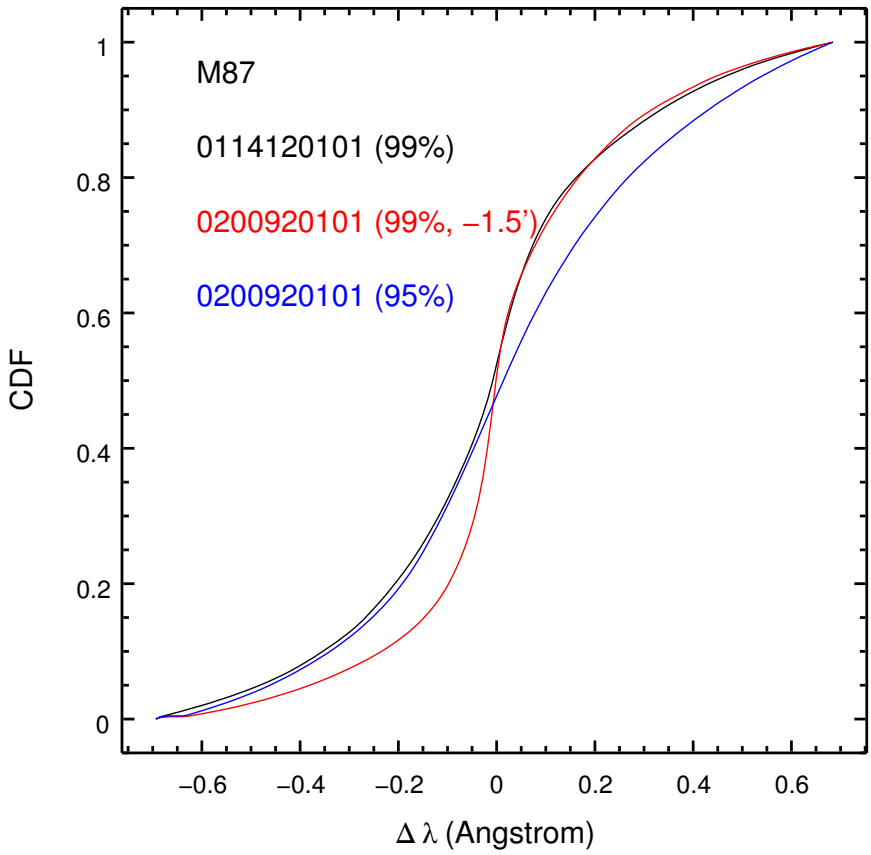

Figure 7.13: The cumulative distribution function (CDF) of the spatial broadening profile of M87. We built the spatial broadening profiles for both two observations (black and red) of the RGS 99%-xpsf source extraction regions. For the second observation (0200920101), a 1.5 arcmin offset is applied so that the extraction region is centred on the peak of the X-ray emission. Moreover, for the second observation, we also built a spatial broadening profile with a narrower 95%-xpsf extraction region (blue) suffering less from central contamination (Figure 7.12).

might be different for different thermal components and/or different ions within the same thermal component. When studying the O VII He-like triplets in the CHEERS sample, Pinto et al. (2016) found the spatial extent of the cooler ICM component is narrower than that of the hotter counterpart, by using two *lpro* model components for the two temperature components. Since in most cases, nitrogen from the hotter component contributes the most to the emission line we observed, thus, applying the same *lpro* model component (mainly determined by the high-temperature lines) to both the hotter and the cooler thermal component should be fine in our case.

7.B.3. RGS background model

In some cases in the CHEERS sample, the modelled background level is even higher than the source continuum level at $\lambda \gtrsim 20$ (Figure 7.1). Thus we check the systematic uncertainties of the modelled background as well. We use A 2029 as an example to compare the observed spectra from an offset observation toward A 2029 with the RGS modelled background.

The outskirts of A 2029 were observed with XMM-*Newton* in 2015. The projected angular distances for the outskirts are ~ 20 arcmin, i.e. at least $\sim 1.3\ r_{500}$. The outskirts of A 2029 were also observed by *Suzaku* and no statistically significant emission is detected beyond 22 arcmin, except for the northern observation (Walker et al. 2012). That is to say, the spectra of the observations toward the outskirts of A 2029 can be considered as background spectra. We used the same data reduction method described in Section 7.2 to screen out the flare time intervals and extracted the RGS spectra in the 99%-xpsf extraction region.

In Figure 7.14, we plot the RGS 1st-order "net" (observed minus modelled background) spectra of the A 2029 southern outskirt (ObsID: 0744411001). If the modelled background spectra is accurate enough, the "net" spectra should be consistent with zero. Above ~26.5 , we see the modelled background spectrum of RGS1 is significantly overestimated. The RGS2 modelled background is more accurate than that of RGS1 above ~26.5 . Therefore, for any source with redshift $z \gtrsim 0.07$, the accuracy of the RGS1 modelled background can be an issue for the N VII Lyα line measurement, if the modelled background level dominates the source continuum level for (redshifted) $\lambda \gtrsim 26.5$.

Last but not least, we take NGC 5846 as an example to show the impact on the abundance measurement if the modelled background were systematically over- or under-estimated. We used the FTOOL task *fcalc* to increase/decrease the values of the entire BACKSCAL column by 10% for the modelled background spectra FITS

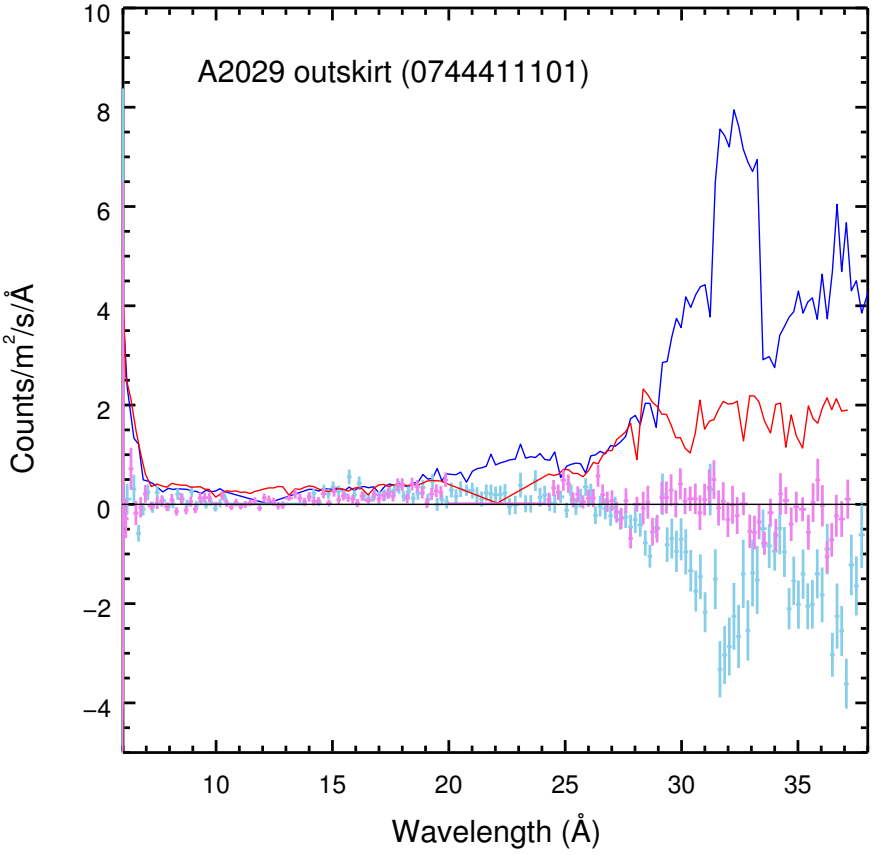

Figure 7.14: The RGS 1st-order spectra of A 2029 outskirt (ObsID: 0744411001). The data with error bars (light blue for RGS1 and violet for RGS2) are the observed background spectra minus the modelled background spectra, which are expected to be around zero, if the modelled background spectra are accurate. The solid lines (deep blue for RGS1 and red for RGS2) are the (subtracted) modelled background spectra obtained with *rgsproc*.

Table 7.7: The best-fit results of the EPIC spectra of NGC 5044 using SPEX v2.06 and v3.03. MOS and pn spectra are fitted simultaneously.

SPEX	v2.05	v3.03	v3.03
SPEXACT	v2.05	v2.05	v3.03
Model	GDEM	3T	3T
C-stat	6502	6210	5635
d.o.f.	1512	1287	1287
Norm.	2.153 ± 0.014	2.218 ± 0.008	2.077 ± 0.023
kT	0.974 ± 0.002	1.043 ± 0.003	0.962 ± 0.004
Si/Fe	0.93 ± 0.14	0.96 ± 0.07	0.79 ± 0.10
S/Fe	1.3 ± 0.3	1.4 ± 0.1	1.1 ± 0.2
Ar/Fe	1.4 ± 0.5	1.3 ± 0.4	1.0 ± 0.3
Ca/Fe	1.5 ± 0.3	1.6 ± 0.3	1.2 ± 0.2

Notes. The normalization in units of 10^{71} m^{-3} refers to the total emission measure. The temperature (in keV) here is where the differential emission measure reaches its maximum.

file. Then we re-analyse the source spectra after subtracting the modified modelled background spectra. Given a 2T model, compared to the results of unmodified modelled background (Table 7.1), the Fe abundance increases/decreases dramatically by $+0.33$ (for 90% BACKSCAL) and -0.15 (for 110% BACKSCAL), respectively. The deviations are significantly larger compared to pure statistical errors. Nevertheless, the abundance ratios of N/Fe and O/Fe are consistent with 3.4 and 1.3, respectively. That is to say, the abundance ratios are robust given a 10% (constant) uncertainty in the modelled background spectra. Similar checks are also performed on other sources with higher modelled background level.

7.C. EPIC spectral analysis of NGC 5044 with SPEX v3.03

The EPIC Si/Fe, S/Fe, Ar/Fe, and Ca/Fe abundance ratios († in Table 7.5) have been reported in Mernier et al. (2016a, their Table D.1). However, an older version of SPEX (v2.05) was used at that time. In the present work, we reanalyze the EPIC spectra with SPEX v3.03. As shown in Table 7.7, the newly obtained abundance ratios are consistent (at a 1σ confidence level) with those reported in Mernier et al. (2016a).

More accurate and complete atomic data (SPEXACT v3.03) are used in SPEX

v3.03 (Section 7.3). The total number of lines has increase by a factor of ~ 400 to reach about 1.8 million in the new version. Consequently, multi-temperature plasma models like GDEM, which has about 20 different normalization/temperature components, is computational expensive for SPEX v3.03. A three temperature (3T) model would be a cheaper alternative for SPEX v3.03. To mimic a Gaussian differential emission measure distribution (GDEM) with a three temperature distribution, we set the temperatures of all three components to be free, the normalization of the main component is also allowed to vary, while the normalization of the low- and high-temperature components are fixed to be half of that of the main component.

MOS and pn spectra are fitted simultaneously. When we use the old atomic database (SPEXACT v2.05), the best-fit C-stat to degree of freedom ratios are 6502/1512 (GDEM in SPEX v2.05) and 6210/1287 (3T in SPEX v3.03), respectively. As expected, the ratio is slightly worse for the 3T model. The degree of freedoms are different mainly due to the fact that the optimal binning algorithm (Kaastra & Bleeker 2016) is different in the two versions of SPEX.

When we use the 3T model and SPEX v3.03, the best-fit C-stat to degree of freedom ratios are 6210/1287 (SPEXACT v2.05) and 5635/1287 (SPEXACT v3.03), respectively. This shows the improvement with the new atomic data.

7.D. IMF weighted SNcc yields and yields of SNIa.

IMF weighted core-collapse supernovae (SNcc) yields are shown in Figure 7.15 with different initial metallicity ($Z_{\rm init}$) and initial mass function (IMF) for the stellar progenitors. Figure 7.16 shows the Type Ia supernovae (SNIa) yields based on theoretical calculations (Iwamoto et al. 1999) and observations of the Tycho supernova remnant (Badenes et al. 2006).

References

Asplund, M. 2005, ARA&A, 43, 481
Badenes, C., Borkowski, K. J., Hughes, J. P., Hwang, U., & Bravo, E. 2006, ApJ, 645, 1373
Badnell, N. R. 2006, ApJS, 167, 334
Barkat, Z., Rakavy, G., & Sack, N. 1967, Physical Review Letters, 18, 379
Böhringer, H. & Werner, N. 2010, A&A Rev., 18, 127
Bulbul, E., Smith, R. K., & Loewenstein, M. 2012, ApJ, 753, 54
Buote, D. A. 2000, MNRAS, 311, 176
Buote, D. A. & Canizares, C. R. 1994, ApJ, 427, 86
Campbell, S. W. & Lattanzio, J. C. 2008, A&A, 490, 769
Chiappini, C., Hirschi, R., Meynet, G., et al. 2006, A&A, 449, L27

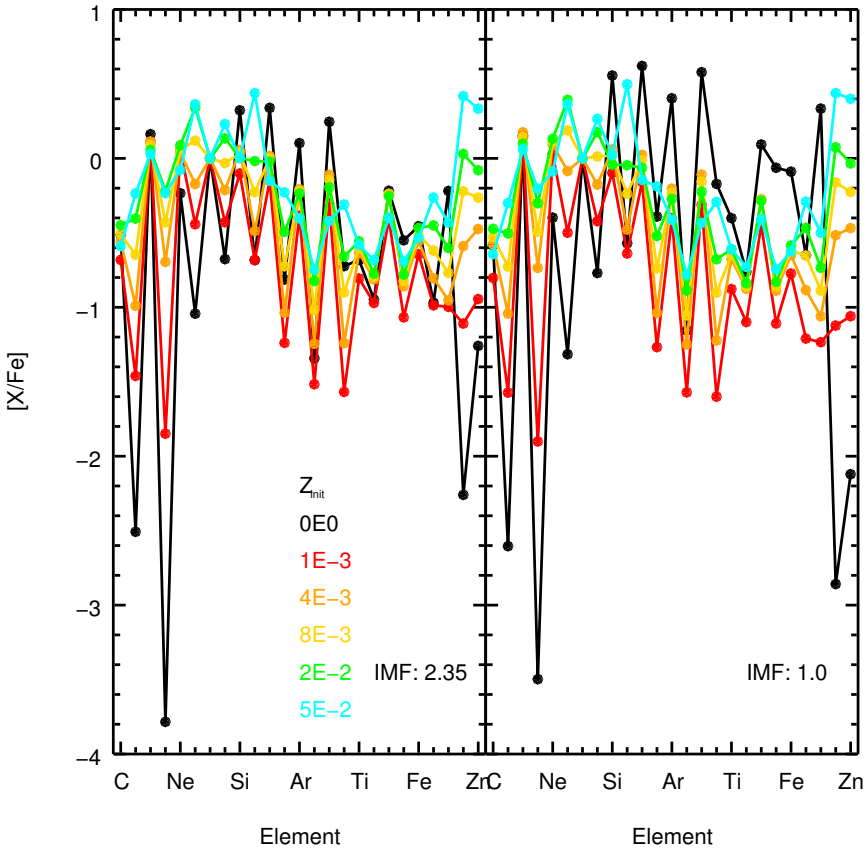

Figure 7.15: IMF weighted SNcc yields, based on the yields table of Nomoto et al. (2013).

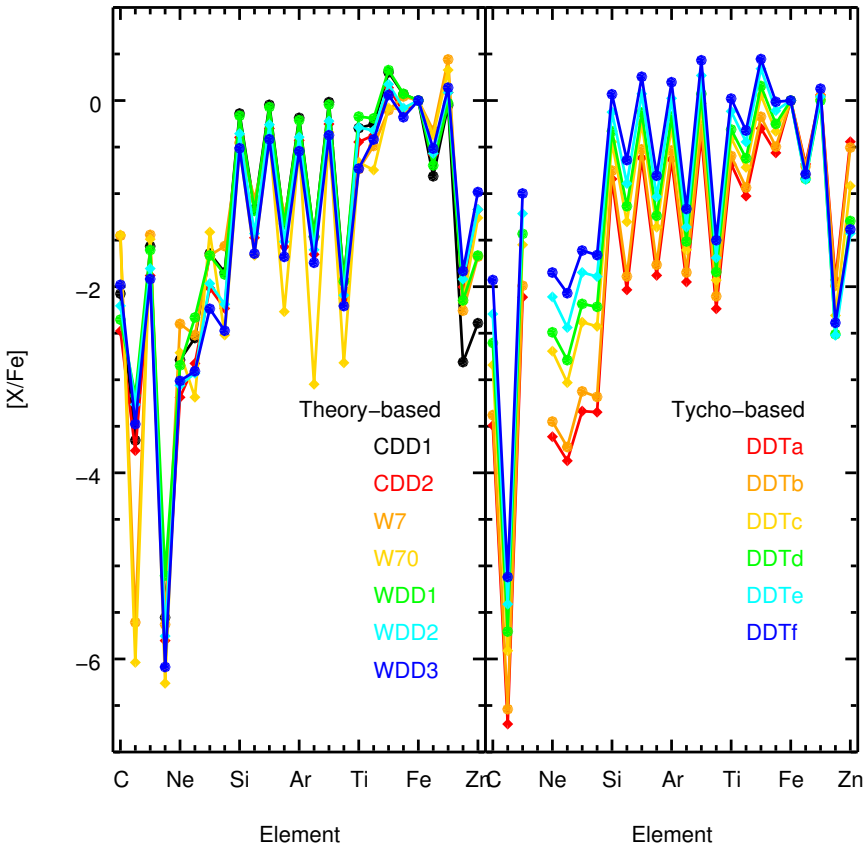

Figure 7.16: Yields from various SNIa models (Badenes et al. 2006; Iwamoto et al. 1999).

de Plaa, J., Kaastra, J. S., Tamura, T., et al. 2004, A&A, 423, 49
de Plaa, J., Kaastra, J. S., Werner, N., et al. 2017, A&A, 607, A98
de Plaa, J., Werner, N., Bykov, A. M., et al. 2006, A&A, 452, 397
den Herder, J. W., Brinkman, A. C., Kahn, S. M., et al. 2001, A&A, 365, L7
Fabbian, D., Nissen, P. E., Asplund, M., Pettini, M., & Akerman, C. 2009, A&A, 500, 1143
Finoguenov, A., Matsushita, K., Böhringer, H., Ikebe, Y., & Arnaud, M. 2002, A&A, 381, 21
Frank, K. A., Peterson, J. R., Andersson, K., Fabian, A. C., & Sanders, J. S. 2013, ApJ, 764, 46
Fujita, Y., Hayashida, K., Nagai, M., et al. 2008, PASJ, 60, 1133
Gil-Pons, P., Gutiérrez, J., & García-Berro, E. 2007, A&A, 464, 667
Grange, Y. G., de Plaa, J., Kaastra, J. S., et al. 2011, A&A, 531, A15
Greene, J. E., Janish, R., Ma, C.-P., et al. 2015, ApJ, 807, 11
Gu, M. F. 2008, Canadian Journal of Physics, 86, 675
Henriques, B. M. B., White, S. D. M., Thomas, P. A., et al. 2015, MNRAS, 451, 2663
Hitomi Collaboration, Aharonian, F., Akamatsu, H., et al. 2017a, Nature, 551, 478
Hitomi Collaboration, Aharonian, F., Akamatsu, H., et al. 2017b, ArXiv e-prints
Israelian, G., Ecuvillon, A., Rebolo, R., et al. 2004, A&A, 421, 649
Iwamoto, K., Brachwitz, F., Nomoto, K., et al. 1999, ApJS, 125, 439
Johansson, J., Thomas, D., & Maraston, C. 2012, MNRAS, 421, 1908
Kaastra, J. S. 2017, Astronomische Nachrichten, 338, 146
Kaastra, J. S. & Bleeker, J. A. M. 2016, A&A, 587, A151
Kaastra, J. S., Mewe, R., & Nieuwenhuijzen, H. 1996, in UV and X-ray Spectroscopy of Astrophysical and Laboratory Plasmas, ed. K. Yamashita & T. Watanabe, 411–414
Kaastra, J. S., Paerels, F. B. S., Durret, F., Schindler, S., & Richter, P. 2008, Space Sci. Rev., 134, 155
Karakas, A. I. 2010, MNRAS, 403, 1413
Kobayashi, C., Umeda, H., Nomoto, K., Tominaga, N., & Ohkubo, T. 2006, ApJ, 653, 1145
Komiyama, M., Sato, K., Nagino, R., Ohashi, T., & Matsushita, K. 2009, PASJ, 61, S337
Landry, D., Bonamente, M., Giles, P., et al. 2013, MNRAS, 433, 2790
Lodders, K. & Palme, H. 2009, Meteoritics and Planetary Science Supplement, 72, 5154
Loewenstein, M. 2013, ApJ, 773, 52
Maeda, K., Röpke, F. K., Fink, M., et al. 2010, ApJ, 712, 624
Mao, J. & Kaastra, J. 2016, A&A, 587, A84
Mernier, F., de Plaa, J., Kaastra, J. S., et al. 2017, A&A, 603, A80
Mernier, F., de Plaa, J., Lovisari, L., et al. 2015, A&A, 575, A37
Mernier, F., de Plaa, J., Pinto, C., et al. 2016a, A&A, 592, A157
Mernier, F., de Plaa, J., Pinto, C., et al. 2016b, A&A, 595, A126
Mollá, M., Cavichia, O., Gavilán, M., & Gibson, B. K. 2015, MNRAS, 451, 3693
Mulchaey, J. S., Kasliwal, M. M., & Kollmeier, J. A. 2014, ApJ, 780, L34
Nandra, K., Barret, D., Barcons, X., et al. 2013, ArXiv e-prints
Nissen, P. E., Chen, Y. Q., Carigi, L., Schuster, W. J., & Zhao, G. 2014, A&A, 568, A25
Nomoto, K., Kobayashi, C., & Tominaga, N. 2013, ARA&A, 51, 457
Pinto, C., Fabian, A. C., Ogorzalek, A., et al. 2016, MNRAS, 461, 2077
Pinto, C., Sanders, J. S., Werner, N., et al. 2015, A&A, 575, A38
Pipino, A., Devriendt, J. E. G., Thomas, D., Silk, J., & Kaviraj, S. 2009, A&A, 505, 1075
Pols, O. R., Izzard, R. G., Stancliffe, R. J., & Glebbeek, E. 2012, A&A, 547, A76

Reddy, B. E., Lambert, D. L., & Allende Prieto, C. 2006, MNRAS, 367, 1329
Renzini, A. & Andreon, S. 2014, MNRAS, 444, 3581
Romano, D., Chiappini, C., Matteucci, F., & Tosi, M. 2005, A&A, 430, 491
Romano, D., Karakas, A. I., Tosi, M., & Matteucci, F. 2010, A&A, 522, A32
Sanders, J. S. & Fabian, A. C. 2006, MNRAS, 371, 1483
Sanders, J. S., Fabian, A. C., Allen, S. W., et al. 2008, MNRAS, 385, 1186
Sanders, J. S., Fabian, A. C., Frank, K. A., Peterson, J. R., & Russell, H. R. 2010, MNRAS, 402, 127
Sanders, J. S., Fabian, A. C., & Smith, R. K. 2011, MNRAS, 410, 1797
Saro, A., Borgani, S., Tornatore, L., et al. 2006, MNRAS, 373, 397
Sato, K., Tokoi, K., Matsushita, K., et al. 2007, ApJ, 667, L41
Schindler, S. & Diaferio, A. 2008, Space Sci. Rev., 134, 363
Shi, J. R., Zhao, G., & Chen, Y. Q. 2002, A&A, 381, 982
Siess, L. 2007, A&A, 476, 893
Smith, R. J., Lucey, J. R., Hudson, M. J., & Bridges, T. J. 2009, MNRAS, 398, 119
Spite, M., Cayrel, R., Plez, B., et al. 2005, A&A, 430, 655
Steenbrugge, K. C., Kaastra, J. S., Crenshaw, D. M., et al. 2005, A&A, 434, 569
Tamura, T., Kaastra, J. S., den Herder, J. W. A., Bleeker, J. A. M., & Peterson, J. R. 2004, A&A, 420, 135
Tamura, T., Kaastra, J. S., Makishima, K., & Takahashi, I. 2003, A&A, 399, 497
Umeda, H. & Nomoto, K. 2002, ApJ, 565, 385
Urdampilleta, I., Kaastra, J. S., & Mehdipour, M. 2017, A&A, 601, A85
Walker, S. A., Fabian, A. C., Sanders, J. S., George, M. R., & Tawara, Y. 2012, MNRAS, 422, 3503
Werner, N., Böhringer, H., Kaastra, J. S., et al. 2006a, A&A, 459, 353
Werner, N., de Plaa, J., Kaastra, J. S., et al. 2006b, A&A, 449, 475
Werner, N., Durret, F., Ohashi, T., Schindler, S., & Wiersma, R. P. C. 2008, Space Sci. Rev., 134, 337
Werner, N., Urban, O., Simionescu, A., & Allen, S. W. 2013, Nature, 502, 656
Werner, N., Zhuravleva, I., Churazov, E., et al. 2009, MNRAS, 398, 23
White, S. D. M., Navarro, J. F., Evrard, A. E., & Frenk, C. S. 1993, Nature, 366, 429
Xu, H., Kahn, S. M., Peterson, J. R., et al. 2002, ApJ, 579, 600
Zhang, Y.-Y., Andernach, H., Caretta, C. A., et al. 2011, A&A, 526, A105